J. Fluid Mech. (2009), *vol.* 623, *pp.* 85–119. © 2009 Cambridge University Press
doi:10.1017/S0022112008005235 Printed in the United Kingdom

The dynamics of the transitional flow over a backward-facing step

F. SCHÄFER, M. BREUER† AND F. DURST

Institute of Fluid Mechanics, University of Erlangen–Nuremberg, Cauerstrasse 4, D-91058 Erlangen, Germany

(Received 24 November 2007 and in revised form 29 October 2008)

The internal flow over a backward-facing step in the transitional regime ($Re_D = 6000$) was studied based on direct numerical simulations. The predictions were carried out with the help of a finite-volume Navier–Stokes solver equipped with a co-visualization facility which allows one to investigate the flow dynamics at high temporal resolution. First, grid-induced oscillations were precluded by a careful grid design. Second, the strong influence of the velocity profile approaching the step was studied and outlined. The main objective, however, was to provide a comprehensive insight into the dynamic flow behaviour, especially oscillations of the reattachment length of the primary recirculation region. The origin of this well-known flapping behaviour of the reattachment line is not yet completely understood. In the present work, the mechanisms leading to the oscillations of the reattachment length were extensively investigated by analysing the time-dependent flow. Besides the oscillations of the primary recirculation region, oscillations of the separation and the reattachment line of the secondary recirculation bubble at the upper channel wall were also observed. The results clearly show that in the present flow case the flapping of the primary reattachment and the secondary separation line is due to vortical structures in the unstable shear layers between the main flow and the recirculation bubbles. Vortices emerging in the shear layers and sweeping downstream convectively induce small zones of backward-flowing fluid at the channel walls while passing the recirculation regions. In the case of the primary recirculation region, the rotational movement of the shear-layer vortices impinging on the lower channel wall was found to cause zones of negative fluid velocity at the end of the recirculation bubble and thus flapping of the reattachment line. In contrast, in the case of the secondary recirculation region, the shear-layer vortices moved away from the upper channel wall so that their rotational movement did not reach the boundary. In this case, the pressure gradients originating from local pressure minima located in the shear-layer vortices were identified as being responsible for the oscillations of the separation line at the upper channel wall. While moving downstream with the shear-layer vortices, the pressure gradients were found to influence the top boundary of the channel and create alternating zones of forward- and backward-flowing fluid along the wall. All of these unsteady processes can best be seen from animations which are provided on the Journal of Fluid Mechanics website: journals.cambridge.org/FLM.

† Present address for correspondence: Department of Fluid Mechanics, Institute of Mechanics, Helmut-Schmidt-University Hamburg, Holstenhofweg 85, D-22043 Hamburg, Germany. Email: breuer@hsu-hh.de

https://doi.org/10.1017/S0022112008005235 Published online by Cambridge University Press

1. Introduction and aim of the work

In many fluid mechanical applications, separating and reattaching flows play an important role. Since the existence of recirculation regions has a significant influence on the heat, mass and momentum transport, it is vital to understand these transport processes and all relevant parameters in order to enhance technical applications further. Therefore, investigations on the separation and reattachment phenomena are of great practical interest. In order to study these features on a fundamental level, the flow over a backward-facing step is generally accepted as a useful test case. Although the geometric configuration is very simple, the resulting flow field behind the step is not. It is characterized by complex flow phenomena including separation and reattachment regions, which makes it attractive for basic investigations of the flow physics and as a benchmark case for numerical methods.

A brief literature survey on backward-facing step flows is given in § 2. Despite the large number of papers dealing with this flow problem, the physical understanding is still incomplete, especially concerning the dynamic processes taking place in the transitional and turbulent regime at higher Reynolds numbers. Under these circumstances, complex time-dependent phenomena such as the well-known oscillations of the reattachment length of the primary recirculation region behind the step, also denoted 'flapping', are observed. Although the term flapping most commonly refers to overall oscillations of separated shear layers, in the present work we concentrate on the flapping of reattachment and separation lines. However, there might be a link between these two forms of flapping, since separated shear layers and the starting and end points of flow separations are not independent entities.

Another well-known phenomenon in transitional and turbulent backward-facing step flows is the development of large-scale vortical structures between the main flow and the recirculation regions owing to instabilities emerging in the shear layers (see § 2). Although it has already been noticed that the vortical structures in the shear layers are linked to the flapping of the primary reattachment line, the specific mechanisms by which the large-scale vortices interact with the recirculation regions, finally leading to the flapping of the reattachment line, has not yet been resolved in detail.

In order to investigate this open question, an internal flow past a backward-facing step in the transitional regime is considered in the present work. This flow case is characterized by a primary recirculation region behind the step, followed by a secondary separation region at the upper wall opposite the step. For the purpose of studying the dynamic behaviour of the step flow, it is essential to visualize and analyse the time-dependent processes at a high temporal resolution. However, up to now only a few rudimentary attempts have been made in this direction. This is related to the fact that predominantly either a rather coarse temporal resolution of the full three-dimensional flow field or time histories at single points were taken into account. To the authors' knowledge, detailed investigations relying on three-dimensional data sets with a high resolution in time are lacking. Hence this issue is the main objective of the present work. It will be exploited to analyse the interaction of the unstable shear layers and the emerging vortical structures with the primary recirculation region in order to identify the precise mechanisms of the flapping behaviour of the primary reattachment line. Furthermore, the issue of the impact of the unstable shear layers on the secondary recirculation region is addressed. The latter is important, since, in contrast to the primary recirculation region, the separation point of the secondary region is not fixed by the geometry.

https://doi.org/10.1017/S0022112008005235 Published online by Cambridge University Press

2. Backward-facing step flow: a brief literature survey

In the past decade, a huge number of publications have become available related to flows over backward-facing steps placed on walls to yield external or internal separated flows. Information for different Reynolds numbers have emerged for two- and three-dimensional flow structures. One of the first investigations on this subject was published by Armaly *et al.* (1983), providing experimental and numerical results for a backward-facing step flow being bounded in a nominally two-dimensional channel. The expansion ratio of this study was $r = 1.9423$, and the channel width was $B = 36h$, where h is the height of the inlet channel in front of the step. In the spanwise direction, the flow was bounded by sidewalls. The investigations covered a wide Reynolds number range of $70 \leqslant Re_D \leqslant 8000$, where Re_D was defined using the hydraulic diameter of the inlet channel $D = 2h$ and the bulk (average) inflow velocity U_b. The oncoming flow was chosen to be that of a fully developed two-dimensional channel flow. Based on experimental investigations of the flow by means of laser-Doppler anemometry, Armaly *et al.* (1983) sub-divided the flow into a laminar regime ($Re_D < 1200$), a transitional regime ($1200 < Re_D < 6600$) and a turbulent regime ($Re_D > 6600$). Besides the primary recirculation region behind the step, Armaly *et al.* (1983) found in some of the Reynolds number ranges additional recirculation regions on the upper channel wall opposite the step as well as on the lower wall downstream of the primary recirculation region. In the range $400 < Re_D < 6600$, variations of the dimensions of the separation and reattachment lines were observed in the cross-stream direction, i.e. along the step; hence the investigated flows showed a clear three-dimensionality, in spite of their occurrence in a nominally two-dimensional channel. According to Armaly *et al.* (1983), the two-dimensionality was lost for a Reynolds number around 400, and it was found that this happened when the first secondary recirculation region formed on the upper channel wall. In addition to experimental studies, Armaly *et al.* (1983) also performed two-dimensional steady flow predictions at $Re_D < 1250$. Up to $Re_D = 400$, good agreement between experimental and numerical results was found. For higher Re_D, the primary separation length was systematically underpredicted compared with the experiment. The authors explained this discrepancy by the occurrence of three-dimensional effects that could not be covered by their two-dimensional computations.

In general, the influence of the three-dimensionality of the flow on the dimensions of the occurring separated flow regions have been investigated extensively, and many authors have used the flow geometry employed by Armaly *et al.* (1983). For instance, Williams & Baker (1997) have studied internal backward-facing step flows in the range $100 \leqslant Re_D \leqslant 800$, using two- and three-dimensional computations. Their three-dimensional simulations resulted in good agreement of the computed separation length with the experimentally found dimensions. In this way, the influence of the three-dimensionality of the flow on the observed separation regions in the centre of the channel was confirmed. The authors found that a transverse flow occurs immediately behind the step that flows from the sidewalls of the channel to its centre. This transverse flow increases in strength with increase in Reynolds number. These kinds of wall jets were confirmed by Chiang & Sheu (1999), Nie & Armaly (2002) and Biswas, Breuer & Durst (2004). Chiang & Sheu (1999) investigated the three-dimensionality for different values of channel width B, providing information in the ranges $2h \leqslant B \leqslant 100h$ and $100 \leqslant Re_D \leqslant 1000$. Through this extensive numerical study, they showed that the influence of the sidewalls on the flow in the centre of the channel increases with increase in Re_D. As the channel width increases, this influence decreases,

https://doi.org/10.1017/S0022112008005235 Published online by Cambridge University Press

and their results demonstrate that the width B needs to be extended to $100h$ in order to avoid disturbances of the two-dimensionality of the flow in the symmetry plane of the channel, at least for their computation at $Re_D = 800$. An increasing influence of the sidewalls was also found in the numerical studies of Biswas *et al.* (2004), who provided two- and three-dimensional computations in the range $10^{-4} \leqslant Re_D \leqslant 800$ and for different expansion ratios $1.9432 \leqslant r \leqslant 3$. Their two-dimensional simulations for $Re_D = 400$ and their three-dimensional computations for the same Re_D agreed very well with experimental data of Armaly *et al.* (1983). For $Re_D > 400$, the authors clearly showed three-dimensional effects on the centre of the flow due to the sidewall influence.

Instabilities of the step flow were investigated numerically by Kaiktsis, Karniadakis & Orszag (1991, 1996), using the same expansion ratio as Armaly *et al.* (1983). The onset of three-dimensionality in the early transitional regime not resulting from sidewall effects was determined by means of direct numerical simulation (DNS) based on a configuration without sidewalls, using periodic boundary conditions in the spanwise direction instead. Above a critical Reynolds number of about 700, a bifurcation of the stationary two-dimensional flow to an oscillating three-dimensional flow was observed. The three-dimensionality started in the shear layers between the main flow and the recirculation regions. Moreover, the authors found a strong influence of the inflow conditions on the developing flow field behind the step. Kaiktsis *et al.* (1996) investigated the stability of the flow in two space dimensions in more detail. In the absence of external perturbations, stationary flows were observed up to $Re_D = 2500$. From $Re_D \approx 700$ upwards the flow was convectively unstable, so that continuous perturbations of even small amplitude and fitting frequency led to a time-dependent flow.

A three-dimensional stability analysis without sidewalls at an expansion ratio of $r = 2$ was performed by Barkley, Gomes & Henderson (2002). In contrast to Kaiktsis *et al.* (1991, 1996), Barkley *et al.* (2002) found a stationary three-dimensional bifurcation of the two-dimensional flow at a critical Reynolds number of $Re_D = 1058$. The critical eigenmode was located within the primary recirculation region behind the step. A centrifugal instability of the flow in the separation bubble was found to be the reason for the bifurcation. The earlier onset of three-dimensionality reported by Armaly *et al.* (1983) and Williams & Baker (1997) was attributed to influences of the sidewalls, which were not considered by Barkley *et al.* (2002).

Recently, Blackburn, Barkley & Sherwin (2008) carried out a detailed investigation of the convective instability and transient growth in flows over a backward-facing step in the Reynolds number range 0–500 (based on the step height and the peak inflow velocity). The transient energy growths of two-dimensional and three-dimensional perturbations imposed on two-dimensional, steady base flows were calculated numerically. The authors found out that three-dimensional disturbances yield slightly larger energy growths than the two-dimensional ones. Additionally, the effect of time-varying white-noise inflow perturbations on the flow was studied. As a result, narrowband velocity perturbations with properties related to the predicted optimal disturbances were observed downstream of the step.

Kaltenbach & Janke (2000) investigated the effect of a swept angle on the transitional separation bubble behind a backward-facing step in the case of an external flow using DNS. In this context, they also performed simulations for the unswept case at $Re_S = 3000$, where Re_S is based on the step height S and the velocity of the external flow. The flow upstream of the step was laminar, and shear-layer transition took place prior to reattachment. Comparing the results for zero sweep from two simulations using either steady inflow conditions or the same velocity profiles with superimposed low-amplitude random disturbances, they found that the flow field downstream of the step is very sensitive to the type of inlet boundary conditions.

https://doi.org/10.1017/S0022112008005235 Published online by Cambridge University Press

Most of the numerical studies have concentrated mainly on the laminar and the early transitional regime. Since these are of minor importance for the present study, we refer to the literature, e.g. Williams & Baker (1997), Chiang & Sheu (1999), Biswas *et al.* (2004), and the references cited therein. DNS and large eddy simulations (LES) in the late transitional and the turbulent regimes are relatively rare. Exceptions can be found, e.g. in Le, Moin & Kim (1997) using DNS and in Friedrich & Arnal (1990) and Métais (2001) relying on LES. Le *et al.* (1997) investigated an external backward-facing step flow at $Re_S = 5100$. At the inlet, a turbulent boundary layer profile was used. The authors observed a quasi-periodic oscillation of the recirculation length with a Strouhal number of $St \approx 0.06$. This temporal fluctuation of the reattachment line (flapping) had already been observed in previous studies by Eaton & Johnston (1980) and Friedrich & Arnal (1990). According to Le *et al.* (1997), large-scale vortical structures developing in the shear layer between the recirculation bubble and the external flow are responsible for the flapping of the reattachment line. Such vortical structures, which were attributed to Kelvin–Helmholtz instabilities in the shear layer, were also described by other authors (see, e.g. Delcayre & Lesieur 1997; Lee & Mateescu 1998; Kaltenbach & Janke 2000; Scarano & Riethmuller 2000; Métais 2001). However, the Strouhal numbers of the Kelvin–Helmholtz vortices in Métais (2001) were found to be significantly larger ($St = 0.23$ for the shedding of the vortices behind the step and $St = 0.12$ after helical pairing) than the Strouhal number for the oscillations of the separation bubble ($St = 0.07$ in the work of Métais 2001). So far the exact mechanisms of the interaction between the vortices, the recirculation region and the main flow have not been resolved. That was the main objective of the present numerical investigation.

3. Numerical method

For the present investigation, the general-purpose computational fluid dynamics (CFD) package FASTEST-3D developed at LSTM Erlangen (Durst & Schäfer 1996; Durst, Schäfer & Wechsler 1996) is applied. With this program both laminar and turbulent steady and unsteady flows including heat and mass transfer can be simulated numerically. The three-dimensional incompressible Navier–Stokes equations expressing the conservation of mass, momentum and energy are solved based on a fully conservative finite-volume discretization on non-orthogonal curvilinear grids with a collocated arrangement of the variables. In order to resolve complex geometries, block-structured grids are used; i.e. the blocks are globally unstructured, but each block can consist of a curvilinear structured grid (Basu *et al.* 2000; Enger *et al.* 2001).

The code is highly optimized for high-performance supercomputers such as vector computers and parallel-vector systems (e.g. NEC SX-8 and Fujitsu VPP 700). Furthermore, it is adapted to symmetric multi-processing (SMP) clusters such as the Hitachi SR8000-F1 using pseudo-vector facilities or the SGI ALTIX. For parallelization, a grid partitioning technique combined with explicit message passing based on MPI is employed. The flow solver has been applied successfully to a long list of engineering and scientific flow problems ranging from external flows around high-speed trains to internal flows in stirred vessels and nearly everything in between (see, e.g. Durst & Schäfer 1996; Durst *et al.* 1996; Grosso *et al.* 1996*a*, *b*; Basu *et al.* 2000; Khier, Breuer & Durst 2000; Enger 2001; Enger *et al.* 2001; Schäfer & Breuer 2002).

3.1. *Governing equations*

An incompressible fluid with constant fluid properties is assumed. The governing equations expressing the conservation of mass and momentum are, in Cartesian

https://doi.org/10.1017/S0022112008005235 Published online by Cambridge University Press

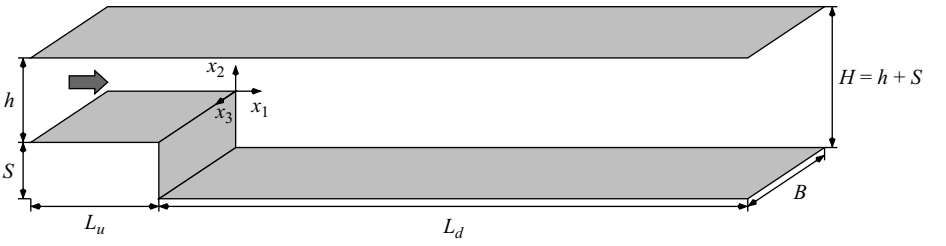

FIGURE 1. Sketch of the flow configuration and the definition of length scales.

coordinates x_j, as follows:

$$\frac{\partial U_i}{\partial x_i} = 0, \tag{3.1}$$

$$\rho\left(\frac{\partial U_j}{\partial t} + U_i\frac{\partial U_j}{\partial x_i}\right) = -\frac{\partial P}{\partial x_j} - \frac{\partial \tau_{ij}^{mol}}{\partial x_i}, \tag{3.2}$$

where $i, j = 1{-}3$. The density of the fluid is given by ρ and the dynamic viscosity by μ. The Cartesian velocity components and the pressure are denoted U_j and P, respectively, and τ_{ij}^{mol} describes the molecular momentum transport, which for a Newtonian fluid can be expressed by

$$\tau_{ij}^{mol} = -\mu\left(\frac{\partial U_i}{\partial x_j} + \frac{\partial U_j}{\partial x_i}\right). \tag{3.3}$$

The only non-dimensional parameter evolving from the governing equations is the Reynolds number. For the flow problem considered, the following definition of Reynolds number is used:

$$Re \;=\; Re_D \;=\; \frac{\rho\, U_b\, D}{\mu}. \tag{3.4}$$

As mentioned before, U_b denotes the bulk velocity of the inlet flow, which corresponds in the case of a fully developed laminar velocity profile to two thirds of the maximum inlet velocity. In the present investigation the notation of Armaly *et al.* (1983) is used, where D is chosen as the hydraulic diameter of the inlet channel, which is equivalent to twice its height, i.e. $D = 2h$ (see figure 1).

3.2. *Discretization and solution method*

FASTEST-3D employs the finite-volume method, where the spatial discretization of all fluxes is based on central differences of second-order accuracy (CDS). Time advancement is performed by a predictor–corrector scheme. A low-storage multi-stage Runge–Kutta method (three sub-steps, second-order accuracy) is applied for integrating the momentum equations in the predictor step. Within the corrector step the Poisson equation for the pressure correction is solved implicitly by the incomplete lower–upper (LU) decomposition method of Stone (1968). Explicit time marching works well for DNS with small time steps, which are necessary to resolve turbulence motion in time. In order to ensure the coupling of pressure and velocity fields on non-staggered grids, the momentum interpolation technique of Rhie & Chow (1983) is used.

https://doi.org/10.1017/S0022112008005235 Published online by Cambridge University Press

4. Definition of the flow problem

In the present study, the internal backward-facing step flow of a Newtonian fluid assuming constant density and viscosity is considered. The flow is in the transitional regime and thus most reliably predicted based on a DNS. The geometry of the flow configuration is sketched in figure 1. Essentially, it consists of a plane channel with a sudden stepwise expansion of the cross-section. The height of the channel in front of the step is denoted h. Downstream of the step the channel height is given by $H = h + S$, where S defines the step height. According to the experimental set-up of Armaly *et al.* (1983) the step height is set to $S = 0.9423h$. Consequently, an expansion ratio $r = H/h = 1 + S/h = 1.9423$ results.

Upstream and downstream of the step, the computational domain has an extension of L_u and L_d, respectively. Since the origin of the coordinate system is located at the edge of the step (see figure 1), the inlet section is at $x_1 = -L_u$, and the outlet section at $x_1 = L_d$. Based on results from the literature, a distance of five times the channel height h upstream of the step expansion is generally sufficient to avoid the backward influence of the inlet on the predicted results past the step (see, e.g., Biswas *et al.* 2004). Hence this value is adopted in the present study.

In order to allow the visualization of the instabilities arising in the shear layers and the interaction of the resulting vortical structures with the recirculation regions, the incoming flow is assumed to be laminar. Thus the flow is expected to become unstable downstream of the step so that the transition to turbulence takes place. That is in contrast to many previous investigations (cf. Le *et al.* 1997; Métais 2001) which considered the fully turbulent regime.

Two different variants are investigated. In the first case, a fully developed laminar channel flow is assumed upstream of the step at the inlet, leading to a standard parabolic velocity profile given by

$$U_1(x_2) = 4\,U_{max}\,\frac{x_2}{h}\left(1 - \frac{x_2}{h}\right). \tag{4.1}$$

Here $U_{max} = 3/2\,U_b$ denotes the maximum velocity of the profile. As mentioned before, the Reynolds number is defined in accordance with the definition (3.4) used by Armaly *et al.* (1983) and set to $Re_D = 6000$. Regarding the notation of Armaly *et al.* (1983), this Reynolds number lies in the late transitional regime.

During the numerical investigations, some doubts arose as to whether in the experimental set-up of Armaly *et al.* (1983) the flow in the channel in front of the step was still in the laminar regime and thus could be described by the parabolic profile. Therefore, a second case is taken into account which mimics the other extremum. Here, a steady block profile with velocity U_b is assumed at the inlet instead of a fully developed laminar channel flow. The corresponding Reynolds number is the same as in the first case.

The upper and lower channel walls as well as the step are treated as impermeable solid walls, and the Stokes no-slip boundary condition is applied. At the outlet of the computational domain ($x_1 = L_d$), a convective boundary condition is used which ensures that vortices are able to approach and pass the outflow boundary without significant disturbances and reflections into the inner domain. The convection velocity required for the formulation of the convective boundary condition is set to the bulk velocity U_b. The outflow length is set to $L_d = 32h$, which agrees with the maximum length used by Biswas *et al.* (2004) and the references cited therein. Additionally, Le *et al.* (1997) have found that for a convective outflow boundary condition the most severe perturbations of statistical flow quantities are limited to a region of about one

https://doi.org/10.1017/S0022112008005235 Published online by Cambridge University Press

Case	Grid	Inflow boundary condition
1	Coarse	Laminar parabolic inflow
2	Fine	Laminar parabolic inflow
3	Fine	Block profile

TABLE 1. Overview of simulation cases.

step height in front of the outflow. In the present case, the flow regions of interest are more than ten step heights away from the outflow, so that the length of the flow domain can be considered sufficient.

In the spanwise direction with width B the flow is assumed to be homogeneous, and thus periodic boundary conditions are applied. Therefore, contrary to the experimental investigations by Armaly *et al.* (1983), the influence of sidewalls is not considered here. Since the main objective of the present study is to investigate the instabilities of the shear layers and the oscillations of the recirculation regions, it is not necessary to take additional sidewalls into account. These phenomena already appear in the simpler homogeneous case as shown, for example, by Le *et al.* (1997) and Métais (2001). Furthermore, the sidewalls substantially change the flow field past the step (see § 2). Hence for the present goals it is more reasonable to investigate the interaction between the shear layers and the recirculation regions without the additional influence of sidewalls.

Under the assumption of homogeneity in the spanwise direction, different suggestions for the channel width B can be found in the literature, e.g. $B = 4S$ in Le *et al.* (1997) and Métais (2001) and $B = 2\pi h$ in Kaiktsis *et al.* (1991). For the choice of an appropriate value for B, different factors have to be taken into account. On the one hand, B has to be sufficiently large in order to catch up the largest flow structures appearing in the spanwise direction. On the other hand, the grid spacing in the spanwise direction has to be sufficiently small in order to resolve the smallest vortical structures. Especially the second issue is neglected in many applications (Breuer 2002). In order to restrict the overall size of the computational grid, both conditions have to be traded off. To guarantee a sufficiently fine resolution in the spanwise direction and to restrict the resulting total grid size to a reasonable measure, a channel width of $B = \pi h$ is assumed in the present work. This is very similar to the value used in Le *et al.* (1997) and Métais (2001) ($B = 4S \approx 3.77h$).

5. Details of the numerical simulations

5.1. *Simulation cases*

The flow problem defined above was treated by means of DNS. Three different time-dependent simulations were carried out based on two grids of different resolution, see table 1. In the following, the simulation runs are enumerated as simulations 1, 2 and 3. Whereas the first simulation is based on a grid with 576 cells in the main flow direction, the other two simulations make use of a significantly finer grid (1088 cells in streamwise direction). Details of the grid design are given in the next section. The difference between simulations 2 and 3 lies in the choice of the inflow velocity profile. For simulations 1 and 2, a fully developed, laminar parabolic profile is used as the inflow condition, whereas in simulation 3 a block profile with the same volume flow rate as in the first two simulations is applied. Simulation 3 was initialized by taking

https://doi.org/10.1017/S0022112008005235 Published online by Cambridge University Press

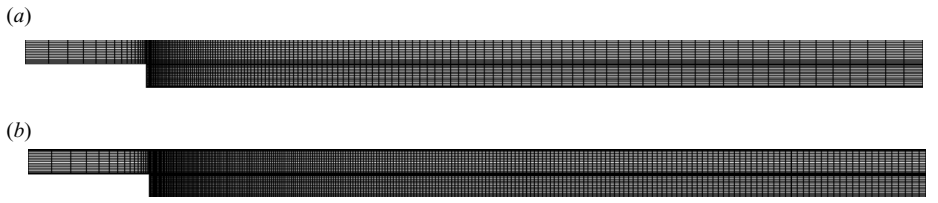

FIGURE 2. Computational grids used for the simulation of the backward-facing step flow (x_1–x_2 plane). Only every fourth grid line is shown. (*a*) Coarse grid. (*b*) Fine grid.

a snapshot of the transient, fully developed flow field of simulation 2 and replacing the parabolic inlet profile by a block profile.

In this paper, simulation 2 is the main application on which most of the discussion will concentrate. The other two cases are taken into account to examine the influence of low grid resolution (simulation 1) or the choice of the inlet boundary condition (simulation 3).

5.2. *Design of the grids*

A suitable computational grid had to be chosen which sufficiently resolves the critical regions of the domain, namely the boundary layers and the evolving free shear layers. An important point is that too large a grid spacing in the main flow direction may cause numerical oscillations, leading to a premature transition of the laminar flow to turbulence (see § 7.1). At high grid Péclet numbers, such oscillations are typical for the CDS scheme applied in the present work.

To eliminate such grid-induced oscillations, two grids with different spacings in the main flow direction are used (see figure 2). The grids contain about 4.5 million control volumes (coarse grid) and 8.7 million control volumes (fine grid). Both grids are orthogonal and offer a refinement of the grid cells next to the walls and at the step. The upper and lower halves of the channel are each discretized with 64 control volumes in the vertical direction. The grid spacing is the smallest ($\Delta x_2 = 0.01h$) along the horizontal line behind the step ($x_2 = 0$) and at the lower and upper walls ($x_2 = -S$, $x_2 = h$). A mild geometric stretching ratio of 1.05 is applied in the vertical direction, resulting in a maximum grid spacing of $\Delta x_2 = 0.02h$. The domain in front of the step is discretized using 64 control volumes in the main flow direction. Behind the step 512 control volumes (coarse grid) and 1024 control volumes (fine grid) are used. The finer grid proved to be necessary to avoid spurious oscillations of the solution. The grid spacing at the step ($x_1 = 0$) is $\Delta x_1 = 0.01h$. At the outflow boundary, the grid spacing is 20 times (coarse grid) or 7 times (fine grid) the spacing at the step. In the homogeneous spanwise direction, an equidistant grid with 64 control volumes is used.

5.3. *Resolution of the boundary layers*

In order to verify that the boundary layers at the walls are sufficiently resolved, the normalized wall distance $\Delta x_2^+ = \Delta x_2 u_\tau / \nu$ of the data points closest to the wall was computed along the bottom channel wall. Here $u_\tau = \sqrt{\tau_w / \rho}$ is the shear stress velocity derived from the wall shear stress τ_w. The stress computations are done based on the flow field averaged both in time and in the spanwise direction. In addition to the wall distance, the normalized grid spacings in the x_1 and x_3 directions are also determined. The results are shown in figure 3.

The curves of Δx_2^+ show fall-offs at the ends of the first Moffat eddy and the primary recirculation region due to vanishing wall shear stress at these points (compare § 7.1.1). In simulation 1 a peak value of about 1.2 is reached, whereas in simulation 2 the

https://doi.org/10.1017/S0022112008005235 Published online by Cambridge University Press

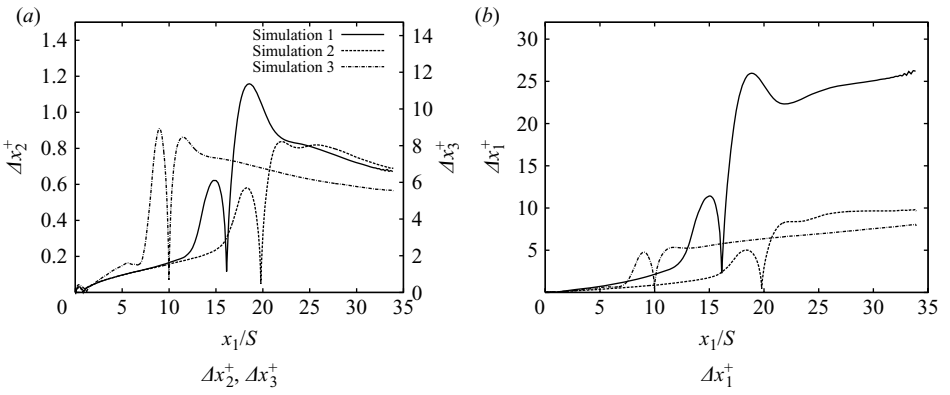

FIGURE 3. Normalized wall distance Δx_2^+ of the data point next to the wall and normalized grid spacings Δx_1^+ and Δx_3^+ along the lower channel wall (flow field averaged in time and in the spanwise direction).

values hardly rise over 0.8. The values for simulation 3 (block inflow profile) are very similar to those for simulation 2 (parabolic profile), but the curves are significantly shifted towards the step for the block profile.

The number of data points with a normalized wall distance below 10 ($N_{x_2^+<10}$) characterizing the viscous sublayer is often used as an indicator for the resolution of the turbulent boundary layer. In the present case we have $N_{x_2^+<10} \geqslant 5$ for simulation 1, $N_{x_2^+<10} \geqslant 7$ for simulation 2 and $N_{x_2^+<10} \geqslant 6$ for simulation 3. The resolution of the viscous sublayer in simulation 1 is reasonable, maybe with the exception of the region behind the primary recirculation bubble in which the main flow impinges at the lower wall. In this respect, the situation for simulations 2 and 3 is better. Here the number of data points next to the wall allows the resolution of the viscous sublayer and is thus considered sufficient.

In addition to the grid spacing in the wall-normal direction, the spacings in the tangential directions also are important for the resolution of flow structures next to the wall. The corresponding values of normalized grid spacings in main flow direction ($\Delta x_1^+ = \Delta x_1 u_\tau/\nu$) and the spanwise direction ($\Delta x_3^+ = \Delta x_3 u_\tau/\nu$) are also depicted in figure 3. The curves for Δx_1^+ reveal the enormous difference between the coarse grid (simulation 1) and the fine grid (simulations 2 and 3) with respect to the grid spacing in the main flow direction. Whereas on the finer grid the values of Δx_1^+ remain below 10, on the coarse grid values around 25 are reached. In the spanwise direction, the normalized grid spacing Δx_3^+ for the fine grid is below 9. The values for the fine grid are of the same order of magnitude as in a DNS of a turbulent backward-facing step flow of Le *et al.* (1997) ($\Delta x_1^+ \approx 10$, $\Delta x_3^+ \approx 15$) and can be considered sufficiently small.

As can be seen from figure 3, the curves for simulation 1 (coarse grid) show some minor oscillations next to the outflow boundary which is located at $x_1/S \approx 34$. The oscillations being confined to a relatively small region before the outflow indicates that the influence of the outflow boundary on the upstream flow does not reach very far. This is in agreement with the results of Le *et al.* (1997) referred to in §4. Moreover, no oscillations are visible for simulations 2 and 3, using the fine grid. From these observations we conclude that the length of our flow domain is long enough to avoid spurious perturbations of the flow region between the primary and the secondary recirculation bubbles, which is of major interest in the present work.

https://doi.org/10.1017/S0022112008005235 Published online by Cambridge University Press

5.4. *Other characteristics of the simulations*

The temporal evolution of the flow field was computed for all three cases over a fairly long period of time. The time step size is normalized with the step size S, and the bulk velocity U_b is chosen as $\Delta t\, U_b/S \approx 0.00495$. This leads to a Courant–Friedrichs–Levy (CFL) number of about 0.7 for simulations 1 and 2 and 0.5 for simulation 3. Hence the stability criterion $CFL \leqslant 2$ for the three-stage Runge–Kutta scheme is fulfilled (Binninger 1989). The convergence criterion was chosen so that the residuals for the mass conservation decrease at least by three orders of magnitude within each time step. To reach convergence, about eight iterations were necessary on average.

Simulation 1 was performed on the Fujitsu VPP 300 parallel-vector computer at the computing centre of the University of Erlangen–Nuremberg. The other two simulations were carried out at the Leibniz Computing Centre Munich, using the SMP-Cluster Hitachi SR-8000 (simulation 2) and the SGI ALTIX system (simulation 3). For simulations 1 and 2, four computing nodes of the respective system were employed. In the case of the third simulation, a total of 16 computing nodes were used. The simulated total time is $t\, U_b/S \approx 2400$ for simulation 1 and $t\, U_b/S \approx 3000$ for simulations 2 and 3. Considering the quantity L_d/U_b as a measure for the flow-through time of the main flow through the channel behind the step, the values above correspond to 71 flow-throughs in the case of simulation 1 and 88 flow-throughs in the case of simulations 2 and 3.

Together with the simulation of the time-dependent flow field, time-averaged values were computed for the velocity $\overline{U_j}$, the pressure $\overline{P}$ and the Reynolds stress tensor $\overline{u_i u_j}$. Additionally, all quantities were averaged in the homogeneous spanwise direction. Averaging was performed over a fairly long time period of $t\, U_b/S \approx 1800$ (simulation 1) and $t\, U_b/S \approx 2000$ (simulations 2 and 3).

6. Visualization method

A co-visualization approach is applied for the visualization of the transient flow at high temporal resolution. Different co-visualization concepts have been described in the literature (Globus 1992; Haimes 1994; Argyris & Schlageter 1996; Grosso *et al.* 1996*a*, *b*; Manzano, Walle & Vandromme 1996). A short overview can be found in Schäfer *et al.* (2005). What all these approaches have in common is that visualization is not performed as a post-processing step after the simulation but rather as a co-processing step parallel to the flow computation. The specific approach employed here is based on the 'extracts' concept of Globus (1992), which was previously used by Haimes (1994). Extracts are sets of physical information extracted from the flow field (e.g. the locations of massless particles traced in the flow field and the values of scalar or vector fields at these locations). These data are transmitted over the network to a graphics workstation (online visualization), where from the same extracts different geometric representations can be created. Since extracts usually need much less storage space than the complete flow solution, this approach has a very large potential for data reduction compared with traditional post-processing.

In the present work, particle-tracking and isosurface techniques are used to generate extracts (streaklines, surfaces of constant pressure, etc.) within the simulation program. For the generation of streaklines, both P-space and C-space particle-tracking schemes have been integrated into the flow solver `FASTEST-3D`. Details of the implementation can be found elsewhere (Schäfer & Breuer 2002). The standard approach for extracting isosurfaces from scalar data given on a structured grid is the marching cubes algorithm

https://doi.org/10.1017/S0022112008005235 Published online by Cambridge University Press

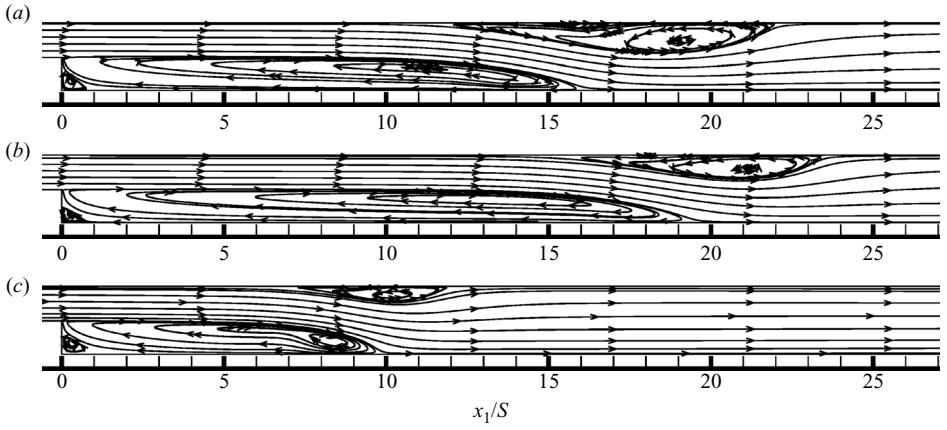

FIGURE 4. Streamlines of the average flow field in a part of the computational domain (inlet at $x_1/S = -5$). (*a*) Simulation 1 (coarse grid, fully developed inflow profile). (*b*) Simulation 2 (fine grid, fully developed inflow profile). (*c*) Simulation 3 (fine grid, block profile at inlet).

originally proposed by Lorensen & Cline (1987). A module for isosurface extraction has been integrated into the flow solver `FASTEST-3D` which adopts this algorithm. For more details please refer to Schäfer *et al.* (2005).

7. Backward-facing step flow

7.1. *Mean flow properties*

In this section we will discuss the average flow field obtained in the different simulation cases. First, the overall structure of the average field will be described. Further, a comparison of the three cases will be given. The results for simulation 2 (fine grid, fully developed inflow profile) will be presented in detail.

7.1.1. *General structure of the average field and comparison between the cases*

The average velocity field for the three cases is shown in figure 4. In all three simulations a large primary recirculation bubble is evolving behind the step. Additionally, there is a secondary recirculation located at the upper wall opposite the step. Both recirculation bubbles are separated from each other by the main flow. However, there are significant differences between the three cases regarding the size of the recirculation regions and the locations of the separation and reattachment points. For the fully developed inflow profile, the fine grid (simulation 2) yields a significant larger reattachment length of the primary recirculation bubble compared with the coarse grid (simulation 1). Moreover, because of the longer primary separation region, the secondary region evolves later on the fine grid but is also much shorter than on the coarser grid. Using a block profile at the inlet (simulation 3), the recirculation regions are much shorter than for the fully developed inflow profile. This qualitative comparison already shows that both the grid resolution and the choice of the inflow condition have a significant impact on the computational results. Obviously, the resolution of the coarse grid is not sufficient to predict the flow field accurately. A more detailed quantitative comparison and a discussion about the origin of the deviations between the three cases will be given below.

In addition to the primary and secondary recirculation regions, smaller structures have been observed in all three simulations. In the corner behind the step, Moffat eddies (Moffat 1964) have developed, as can be seen in figure 4. Moffat eddies

https://doi.org/10.1017/S0022112008005235 Published online by Cambridge University Press

	x_r/S	$x_{s,1}/S$	$x_{s,2}/S$	$x_{s,3}/S$	$x_{s,4}/S$	$x_{p,1}/S$	$x_{p,2}/S$
Simulation 1	16.15	11.19	22.45	14.73	16.95	0.896	0.042
Simulation 2	19.79	14.82	23.92	17.59	18.45	0.810	0.037
Simulation 3	10.02	6.79	12.22	8.63	9.34	1.225	0.047

TABLE 2. Location of the separation and the reattachment points of the average flow field. See figure 5 for the notation used.

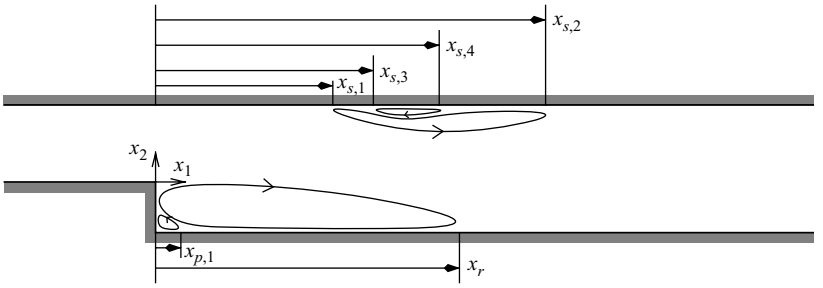

FIGURE 5. Schematic drawing of the location of the different separation regions and definition of the notation used in the text: p denotes the primary recirculation region, whereas s denotes the secondary recirculation. Note that only the largest Moffat eddy in the corner behind the step is shown. The smaller Moffat eddies are enumerated consecutively; i.e. the next smaller Moffat eddy is denoted by $x_{p,2}$.

have also been found by, e.g., Biswas *et al.* (2004). Theoretically, there is an infinite series of Moffat eddies of decreasing size located in the corner behind the step. In the present work, the resolution of both grids is sufficient to resolve two eddies of this infinite series (see table 2). Another small eddy can be found between the secondary recirculation bubble and the top wall, which is only weakly pronounced but clearly present in the average field. The thickness d of this structure is $d/S \approx 0.04$ (simulation 2) and $d/S \approx 0.05$ (simulation 3).

The general structure of the average field is summarized schematically in figure 5. In addition to the primary and secondary recirculation regions there are smaller eddies in the corner behind the step and between the secondary separation bubble and the top wall, as mentioned earlier. However, these smaller structures are of minor importance. The dominant structures are the two large separation regions and the main flow which is passing between them.

For a detailed quantitative investigation, the positions of the separation and reattachment points of the average flow along the top and the bottom wall were determined. For this purpose, the points at which the wall shear stress $\tau_w = -\mu \partial \overline{U}_1/\partial x_2$ changes its sign were computed. The notation introduced in figure 5 is used for designating the distance of the different separation and reattachment points from the step. The results are summarized in table 2. Quantitatively, there is a considerable difference between the simulations. The primary reattachment length x_r on the fine grid was found to be about 23 % larger than on the coarser grid. The distance of the separation point of the secondary recirculation bubble from the step is 32 % longer. In absolute numbers, the points of separation and reattachment are shifted by $3.6\,S$ (x_r and $x_{s,1}$).

The large deviations between simulations 1 and 2 can be attributed to grid-induced oscillations present in the flow solution on the coarser grid of simulation 1. This

https://doi.org/10.1017/S0022112008005235 Published online by Cambridge University Press

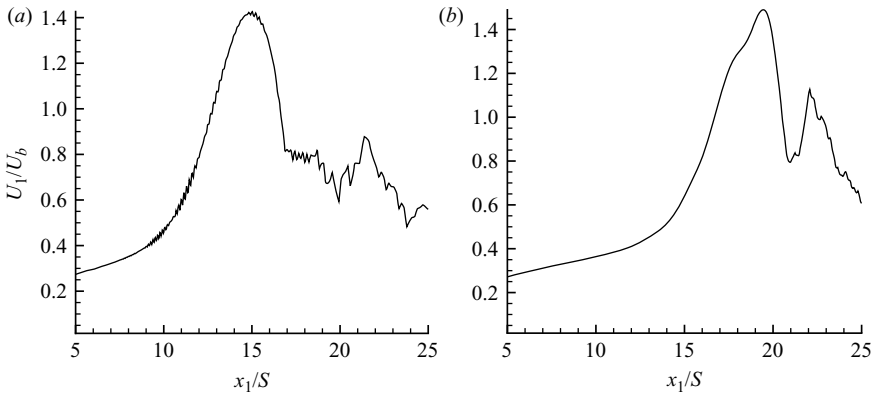

FIGURE 6. Horizontal profile of the transient velocity U_1 along the line $x_2 = 0$ at an arbitrary instant of time (flow field averaged in the spanwise direction). (*a*) Simulation 1. (*b*) Simulation 2.

is shown in figure 6 based on horizontal profiles of the transient velocity U_1 along the line $x_2 = 0$. The diagrams clearly show that on the coarse grid there are strong oscillations of the velocity field downstream of $x_1/S \approx 9$. The wavelength of these oscillations is given by two times the grid spacing in the x_1-direction. In contrast, on the fine grid of simulation 2 no grid-induced oscillations have been observed. The oscillations on the coarse grid represent a numerically induced perturbation which changes the flow field considerably. As will be shown in § 7.2, the shear layers between the main flow and the two recirculation regions are convectively unstable in the present flow configuration. Thus, small fluctuations of the flow field next to the step exhibit an exponential growth with increasing distance from the step, finally leading to a turbulent flow. The grid-induced oscillations on the coarse grid seem to be amplified in the unstable shear layers so that there is an earlier transition from laminar to turbulent flow. As a consequence, the turbulent transport in the vertical direction leads to a shortening of the primary reattachment length, which also causes an earlier development of the secondary separation bubble.

Looking at the results of simulation 3 in table 2, the primary and secondary separation and reattachment lengths (x_r, $x_{s,1}$ and $x_{s,2}$) are only about half as long as the corresponding lengths for simulation 2. On replacing the fully developed inflow profile by a block profile, drops of the separation and reattachment lengths by 49 % (x_r and $x_{s,2}$) and 54 % ($x_{s,1}$) have been observed in the resulting long-term average field. Owing to the block profile at the inlet, there are larger velocity gradients in the wall-normal direction than in the case of a parabolic profile. This is likely to accelerate the growth of shear-layer instabilities and thereby to cause an earlier transition to turbulence. Similar to simulation 1, this explains why in simulation 3 considerably shorter separation and reattachment lengths have been obtained.

The sensitivity of the step flow to the inflow conditions has also been reported by, e.g., Kaiktsis *et al.* (1991) and more recently by Blackburn *et al.* (2008). It is important to note that the above values of the separation and reattachment lengths in simulation 3 are the long-term average values. In the short term, i.e. while the transient perturbation due to the change from the parabolic to the block profile is still effective, significantly shorter recirculation regions have been observed. While the perturbation was swept downstream during the course of simulation 3, the size of the recirculation regions was found to increase extremely slowly, showing that the

https://doi.org/10.1017/S0022112008005235 Published online by Cambridge University Press

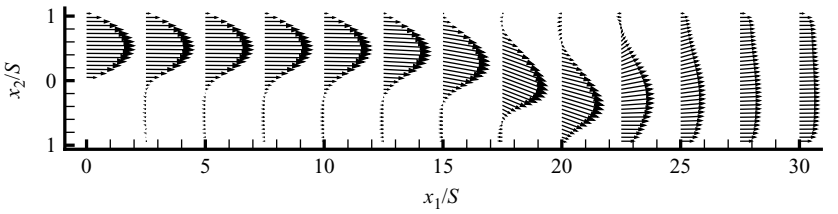

FIGURE 7. Profiles of the average flow velocity at different streamwise positions x_1/S (simulation 2).

backward-facing step flow requires a very long time to settle again after some transient perturbation has occurred. This indicates that repeated transient perturbations at the inlet may lead to much smaller recirculation regions behind the step. This finding is in accordance with investigations based on time-dependent turbulent inlet profiles, which also show considerably shorter recirculation regions than in the present work (see, e.g. Le *et al.* 1997).

This has to be taken into account when comparing the results with the experimental data of Armaly *et al.* (1983). The quantitative values of the separation and reattachment lengths in the experiment ($x_r/S \approx 6.1$, $x_{s,1}/S \approx 3.9$ and $x_{s,2}/S \approx 8.5$) differ considerably from the results of simulation 2. However, it is not completely clear whether the flow in Armaly *et al.* (1983) was laminar or transitional in front of the step at $Re_D = 6000$. The Reynolds number in the inlet channel is about 2200 (based on the centreline velocity and $h/2$); so it is very likely that the flow was not laminar in the experiments. In the case of intermittent transitional flow, there are repeated transient perturbations which, according to the discussion above, will lead to significantly shorter recirculation regions than those observed in the laminar case of simulation 2.

To summarize the above findings, one can assert that there is a distinct influence of the inlet boundary condition on the resulting average flow field. Moreover, the flow considered in this work is very sensitive to grid-induced oscillations, which change the resulting flow field considerably and thus have to be avoided by a careful grid design as done for the fine grid. For transitional flow, an insufficient grid resolution can lead to a premature transition from laminar to turbulent flow and thereby to an underprediction of the separation and reattachment lengths.

The remainder of this paper concentrates on the results of simulation 2. Since the grid resolution of simulation 1 was found to be insufficient, this case will not be considered further. Simulation 3 has been taken into account to examine the influence of the inflow boundary condition on the separation and reattachment lengths of the average flow. Therefore, a detailed discussion of the results of simulation 3 is beyond the scope of this paper.

7.1.2. *Analysis of the mean flow field (simulation 2)*

In this section, the mean flow field obtained in simulation 2 is discussed in more detail. Figure 7 depicts velocity profiles at different positions x_1/S. Over a long distance behind the step, the main flow moves between the upper channel wall and the primary recirculation region. The flow is confined by the wall and the separation bubble in such a way that the profile changes only very little down to $x_1/S = 12.5$. In particular, the maximum velocity does not decrease significantly. However, when passing the region between the two separation bubbles ($15 \leqslant x_1/S \leqslant 24$), the cross-section of the main flow increases. As a consequence, due to mass conservation the

https://doi.org/10.1017/S0022112008005235 Published online by Cambridge University Press

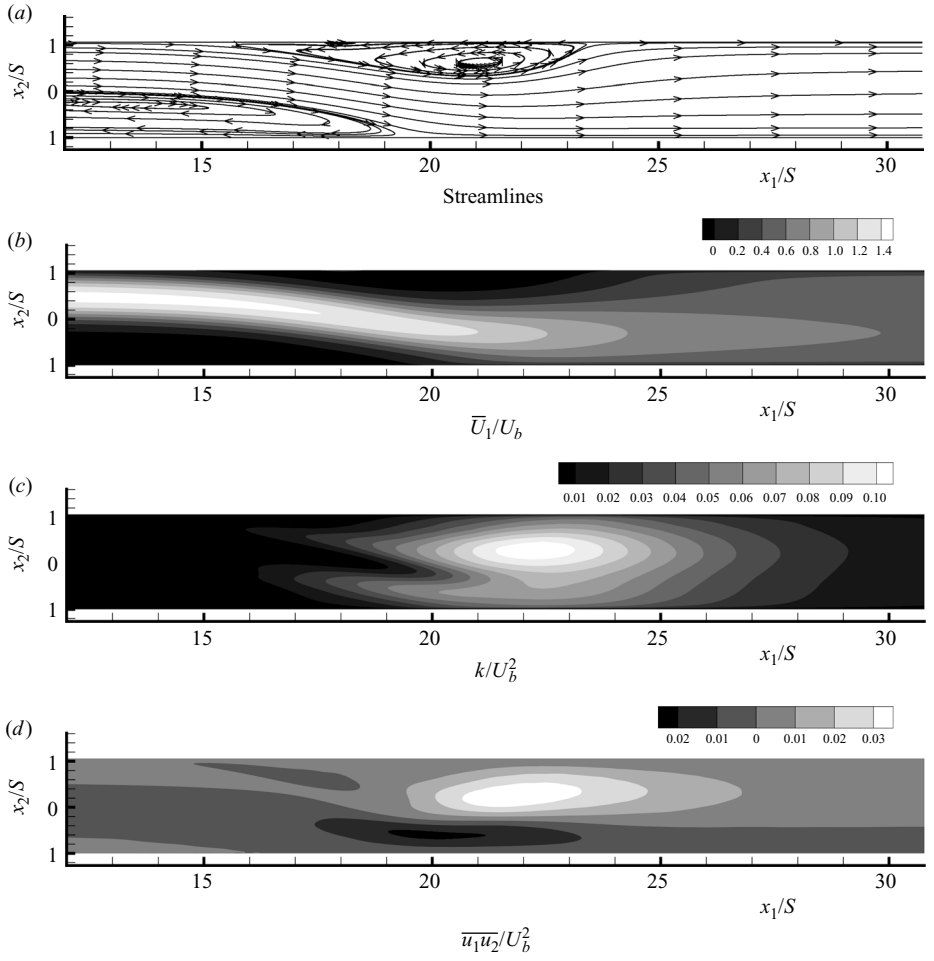

FIGURE 8. Average flow field and distribution of turbulent kinetic energy and Reynolds shear stress for simulation 2 (part of the computational domain).

maximum velocity decreases. Downstream of the recirculation zones ($x_1/S \geqslant 24$), the main flow spans the full cross-section of the channel and the velocity profiles flatten, indicating that the flow is turbulent in this region.

A similar picture is obtained when looking at the distribution of the average velocity field $\overline{U}_1$ in the x_1–x_2 plane shown in figure 8(*b*). The velocity of the main flow decreases significantly between the two recirculation regions, while the cross-section of the flow increases. This is associated with the pressure field (not shown here). In the region between the recirculation bubbles, a streamwise pressure gradient is present, which leads to deceleration of the flow. Downstream of the recirculation zones, the pressure level is substantially higher than upstream.

The transition from laminar to turbulent flow takes place in the region between the two recirculation zones. Evidence for this can be found by examining the spatial distribution of the relevant Reynolds stresses $\overline{u_i u_j}$. Since the spatial distribution of all normal Reynolds stresses are similar, only the distribution of the turbulent kinetic

https://doi.org/10.1017/S0022112008005235 Published online by Cambridge University Press

energy $k = (1/2)\overline{u_i u_i}$ is depicted in figure 8(*c*). The values of $\overline{u_1 u_1}$ rise significantly for $x_1/S > 15$, starting in the two shear layers between the main flow and the recirculation regions. The other normal stresses, $\overline{u_2 u_2}$ and $\overline{u_3 u_3}$, behave in a similar way, but the absolute values remain below those of $\overline{u_1 u_1}$. Accordingly, the dominating component of the Reynolds stress tensor is the normal stress $\overline{u_1 u_1}$. All three normal stresses reach their maximum between the main flow and the secondary recirculation bubble, and further downstream they drop off again. As a consequence, the turbulent kinetic energy behaves similarly. In particular, the production of turbulent kinetic energy starts in the shear layers between the main flow and the two regions of flow separation.

Regarding the shear stresses, only $\overline{u_1 u_2}$ (figure 8*d*) makes a contribution to the turbulent momentum transport. The values of $\overline{u_1 u_3}$ and $\overline{u_2 u_3}$ found numerically lie at least two orders of magnitude below the values of $\overline{u_1 u_2}$. This is in accordance with the expectation that in the homogeneous x_3-direction there is no u_1 and u_2 momentum transport on average.

7.2. *The dynamics of the flow field*

The instantaneous flow field was analysed in detail using the simulation data of case 2. For that purpose, the co-visualization analysis tools described in § 6 were used. First, the instantaneous behaviour of the recirculation regions was thoroughly investigated, leading to the finding that the separation and reattachment lines are subject to strong temporal fluctuations. Vortical structures emerging from the instabilities in the shear layers are found to be the reason for these temporal oscillations of the recirculation regions. Finally, the interaction between the shear-layer vortices and the recirculation regions was studied in detail, leading to new findings concerning their relation. Furthermore, since the instantaneous behaviour of the flow cannot be appropriately represented by series of figures, animation sequences for the same are available online (videos 1 to 10, journals.cambridge.org/FLM).

7.2.1. *Temporal development of the recirculation regions*

In order to investigate instantaneous phenomena in the region of the separation and reattachment zones in detail, isosurfaces of the vanishing streamwise velocity component are considered. These isosurfaces of the isovalue $U_1 = 0$ allow for a straightforward distinction between regions with positive fluid velocities ($U_1 > 0$) and negative velocities ($U_1 < 0$); i.e. recirculation regions are directly identified. The extraction of the isosurfaces from the instantaneous flow field is carried out in parallel with the simulation itself applying the co-visualization methods described above.

Figure 9 depicts the temporal development of the recirculation regions for about a complete period to be discussed below. The primary recirculation region can be detected at the lower channel wall, whereas the secondary region is found at the upper wall. In the temporal development, the recirculation regions show quasi-periodic oscillations which lead to distinct fluctuations of the separation and reattachment lines. Additionally, the figure clearly shows that in the separation region of the secondary recirculation at the upper wall zones with backward and forward flowing fluid alternately occur. These zones move downstream in time until they reach the rear turbulent region of the secondary recirculation and merge with this part of the flow. After a certain time interval, a new region of backward-flowing fluid emerges again further upstream, resulting in a sudden shift of the first separation point of the mean flow at the upper channel wall. Furthermore, analogous oscillations of the reattachment zone of the primary recirculation at the lower wall can clearly be seen.

https://doi.org/10.1017/S0022112008005235 Published online by Cambridge University Press

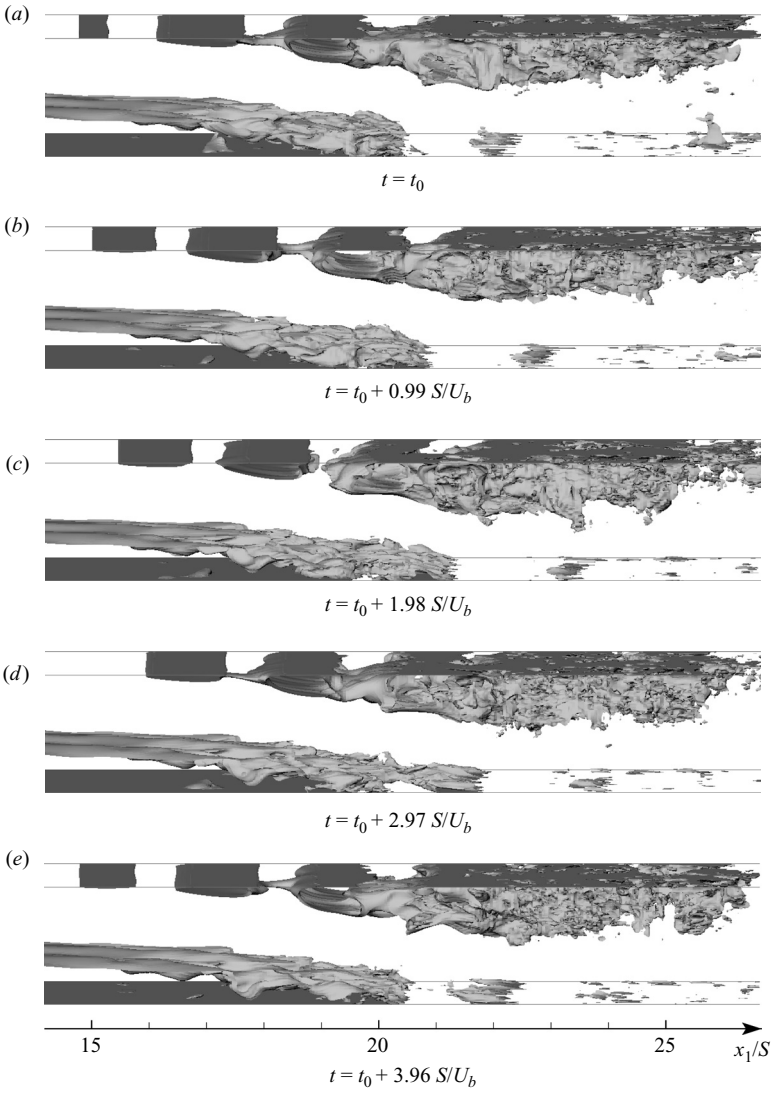

FIGURE 9. Temporal development of the reattachment region of the primary recirculation as well as the separation region of the secondary recirculation visualized by isosurfaces of the vanishing streamwise velocity component (initial time instant t_0 arbitrarily chosen). A corresponding animation can be found online (video 1).

In figure 9(a–c) an increase of the extension of the recirculation region is obvious, leading to a downstream movement of the reattachment region in time. Then with increasing time, however, a region characterized by negative fluid velocity separates from the primary recirculation zone and is convected downstream. Owing to this effect, the reattachment point suddenly jumps upstream. This phenomenon is known in the literature and denoted flapping behaviour of the primary reattachment line (see also § 2).

The phenomena observed are quasi-periodic processes, which are depicted in figure 10 for a longer time interval. The graphs represent the temporal evolution of the separation and reattachment points along both channel walls, whereas the

https://doi.org/10.1017/S0022112008005235 Published online by Cambridge University Press

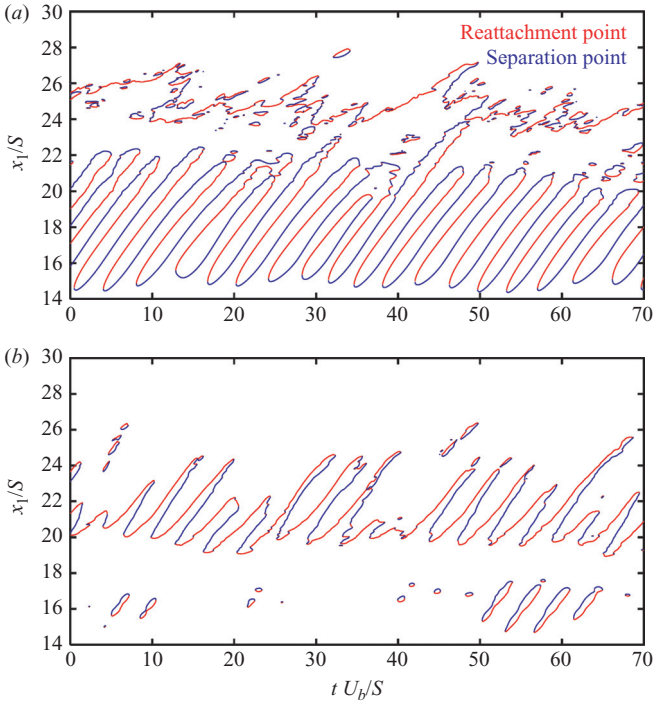

FIGURE 10. Temporal evolution of the separation and reattachment points of the flow at the upper and the lower channel wall. Velocity field averaged in the spanwise direction, initial time instant $t = 0$ arbitrarily chosen, (a) upper wall and (b) lower wall without considering the Moffat vortices.

instantaneous flow field is averaged in the spanwise direction in order to generate a clearer view. Furthermore, for the sake of an improved visibility, the separation and reattachment points resulting from the Moffat vortex in the corner of the step is not included. The time histories clearly show the temporal oscillations of the recirculation regions. Looking at a certain instant in time and moving vertically upwards in the diagrams, the complex spatial structure of the recirculation region becomes obvious. At each instant of time it consists of a series of multiple separation and reattachment points. Between a separation point and a succeeding reattachment point a region comprising negative streamwise fluid velocities U_1 can be found. Correspondingly, each reattachment point is followed by a zone of positive fluid velocity until it ends by the subsequent separation point. The time histories in figure 10 vividly demonstrate how the regions of negative U_1 velocity move downstream in time and how upstream new regions are emerging before the old ones have completely disappeared. Furthermore, it is visible that at the upper wall for $x_1/S < 20$ both the temporal and spatial behaviours of the separation and reattachment points are highly ordered, whereas the order is more or less lost completely for the region $x_1/S > 20$. The reattachment region of the secondary recirculation at the upper wall exhibits distinct spatial and temporal fluctuations which are due to turbulent fluid motions. Moreover, at the lower wall small, relatively short-lived regions of positive fluid velocity can be found within the primary recirculation region. This feature occurs from time to time in an irregular manner in the range $14 < x_1/S < 18$. In the time-averaged flow these structures cannot be observed, which is in accordance with

https://doi.org/10.1017/S0022112008005235 Published online by Cambridge University Press

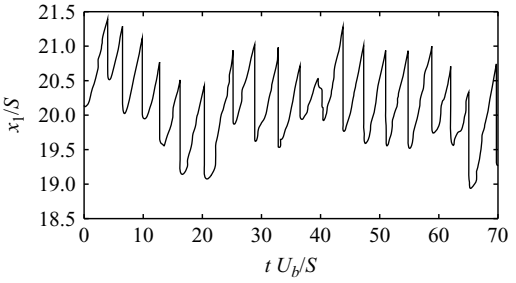

FIGURE 11. Time history of the location of the reattachment point of the primary recirculation region.

their sporadic and irregular appearance. Finally, it can be seen in figure 10 that the recirculation regions at both walls possess only a restricted lifetime. Since the flow past the two recirculation regions continuously transforms to a plane channel flow, no further recirculation regions are observed beyond $x_1/S \approx 28$.

A more detailed analysis yields the finding that the length of the period of the oscillation and also the spatial development of the separation and reattachment lengths underlie certain fluctuations. In order to determine a mean oscillation frequency, the average period length was determined by taking 29 cycles into account. The resulting mean Strouhal number of the oscillations for the separation point of the secondary recirculation region and the reattachment point of the primary recirculation region is $St = f\,S/U_b \approx 0.266$, where f denotes the frequency of the oscillations.

A closer look at the time history of the reattachment length of the primary recirculation region taking the shortest distance in the range $x_1/S > 17$ into account (figure 11) yields a saw-toothed behaviour which is characterized by a nearly linear increase in time followed by a sudden drop. These observations can be explained by the continuous increase of the recirculation region in time and the succeeding separation of a region with negative streamwise velocity visible in the isosurface representation in figure 9. The spatial fluctuations of the reattachment length are of the order of one step height. This outcome qualitatively agrees well with the observations by Le *et al.* (1997), who also observed a saw-toothed behaviour of the reattachment length of the primary recirculation region. Since another flow configuration (external flow past a step in the turbulent regime using a turbulent boundary layer profile as inlet condition) was investigated by Le *et al.* (1997), quantitative agreement cannot be expected. The authors explained the saw-toothed behaviour by large-scale vortical structures emerging from the roll-up of the shear layer past the step. Therefore, this phenomenon will be investigated in more detail in the next section.

7.2.2. *Vortical structures and instabilities in the shear layers*

Vortex cores are often, though not always, characterized by local pressure minima. The pressure forces acting inwards compensate for the outward-acting centrifugal forces resulting from the vortex rotation. To investigate the existence of large-scale vortical structures, regions of local pressure minima were searched for. For that purpose, isosurfaces of low pressure values were considered which were extracted at high temporal resolution in parallel with the simulation.

The temporal evolution of the extracted flow structures is depicted in figure 12. Obviously, tubelike structures occur in the shear layers between the main flow and the two recirculation regions. In the inner part of these structures a local pressure

https://doi.org/10.1017/S0022112008005235 Published online by Cambridge University Press

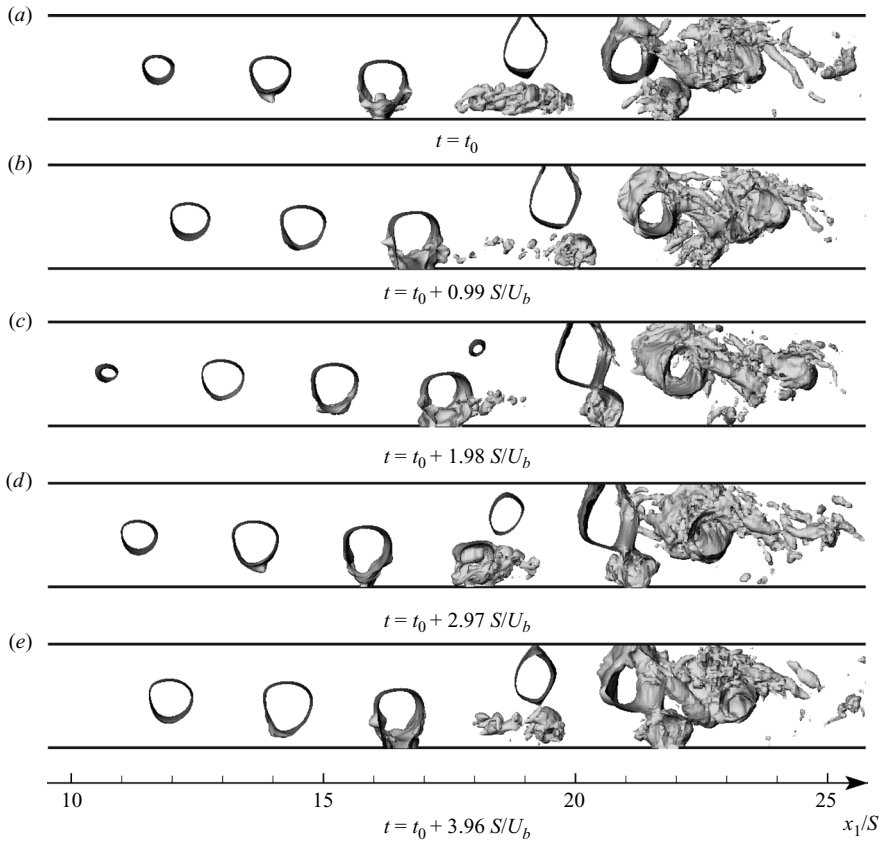

FIGURE 12. Temporal development of the vortical structures spanning the same time interval as depicted in figure 9, visualized by isosurfaces of low pressure values. A corresponding animation can be found online (video 2).

minimum is found, indicating that the structures can be characterized as vortex cores. This statement is confirmed by additional visualizations using particle tracking to be discussed below (see figure 14). As visible from an additional top view (not shown here), the vortical structures are initially two-dimensional without a significant variation in the spanwise direction. Reaching the end of the primary recirculation region, first variations in the homogeneous x_3-direction start to grow. At the end of the secondary recirculation region, significant variations arise due to turbulent fluctuations. The vortices loose their original orientation in the spanwise direction, and structures aligned with the other spatial directions can be detected.

Considering the temporal development of the structures in figure 12, it can be noticed that the vortices are transported downstream by convection, whereupon after a certain time new vortices evolve in the upstream region. The mean convection velocity derived from the isosurface data is about $0.63\,U_b$ and $0.57\,U_b$ for the vortices in the lower shear layer and the upper shear layer, respectively. The two velocities differ only marginally. The structures evolving in the lower shear layer hit the bottom wall at the end of the primary recirculation region, leading to a complex interaction between the vortex, the recirculation region and the wall. This can be realized by a significant change of the isosurface and thus the pressure distribution in this area.

https://doi.org/10.1017/S0022112008005235 Published online by Cambridge University Press

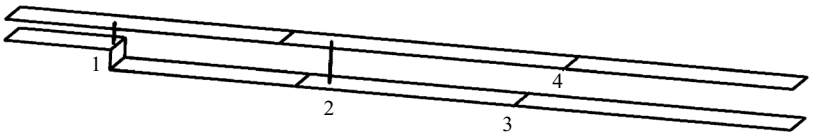

FIGURE 13. Spatial arrangement of particle sources. Source zone 1: vertical, $x_1/h = -0.2$, $x_3/h = \pi/2$, $N_{pos} = 100$ (before step). Source zone 2: vertical, $x_1/h = 10.0$, $x_3/h = \pi/2$, $N_{pos} = 100$ (past step). Source zone 3: horizontal, $x_1/h = 19.0$, $x_2/h = -0.9323$, $N_{pos} = 50$ (end of primary recirculation). Source zone 4: horizontal, $x_1/h = 21.25$, $x_2/h = 0.99$, $N_{pos} = 50$ (in secondary recirculation). N_{pos} denotes the number of particle sources.

The generation of the vortical structures in the shear layers was investigated in detail using streakline visualizations. For that purpose, massless particles were regularly injected into the flow at certain source positions. Then their movement through the instantaneous flow field was tracked using the C-space method mentioned above. The source positions used are sketched in figure 13. Considering solely particles released at the same source yields the corresponding streaklines.

If particles are released from source zone 1 directly in front of the step, the flow is found to be two-dimensional and laminar in a large area past the step (not shown here). Initial three-dimensional flow structures and thus the first hints for the transition process can be observed in the zone between both recirculation regions. The transitional character of the flow in this area is also obvious in the distribution of the turbulent kinetic energy discussed above. The zone in which transition takes place is visualized in figure 14 in a zoomed view. As visible in the side view, the shear layers start to roll up, resulting in striking vortex structures. The colour coding using the normalized pressure at the position of the particles confirms the existence of local pressure minima in the vortex cores. Hence the isosurfaces of low pressure level depicted in figure 12 indeed correspond to vortex structures as expected.

In the literature, often the Kelvin–Helmholtz instabilities were identified as the main mechanism for the generation of the shear-layer vortices (compare § 2). The roll-up of the shear layers as visible in figure 14 is a typical feature of such instabilities. First it starts with a moderate vertical widening of the streaklines, which are in principle aligned with the main flow direction prior to this event. The flow structures generated are convected downstream, whereby the widening increases and due to vertical velocity gradients in the shear layers transforms more and more into a roll-up process. During this process, the vortical structures in the upper shear layer between the main flow and the secondary recirculation remain initially highly ordered, whereas strong deformations of the vortices in the lower shear layer already take place at an earlier stage. These vortices are strongly stretched between the downward-directed main flow and the primary recirculation region. Nevertheless, they preserve their vortical character, as is obvious from the isosurface representation in figure 12 in the range $18 < x_1/S < 22$. Finally, the top view in figure 14(*b*) confirms that the three-dimensionality of the flow starts with the roll-up of the vortices.

In order to investigate the roll-up phenomenon more deeply, the source region 2 was taken into account, which is located much closer to the zone of vortex roll-up (compare figure 13). A snapshot of the streaklines released at source zone 2 is depicted in figure 15 using colour coding according to the dominating normal stress component $\overline{u_1 u_1}$. The distribution of $\overline{u_1 u_1}$ affirms that the increase of the statistical fluctuations in the shear layers already addressed in § 7.1 is mainly due to the instantaneous roll-up of the vortices. As can be observed in animations produced over a time

https://doi.org/10.1017/S0022112008005235 Published online by Cambridge University Press

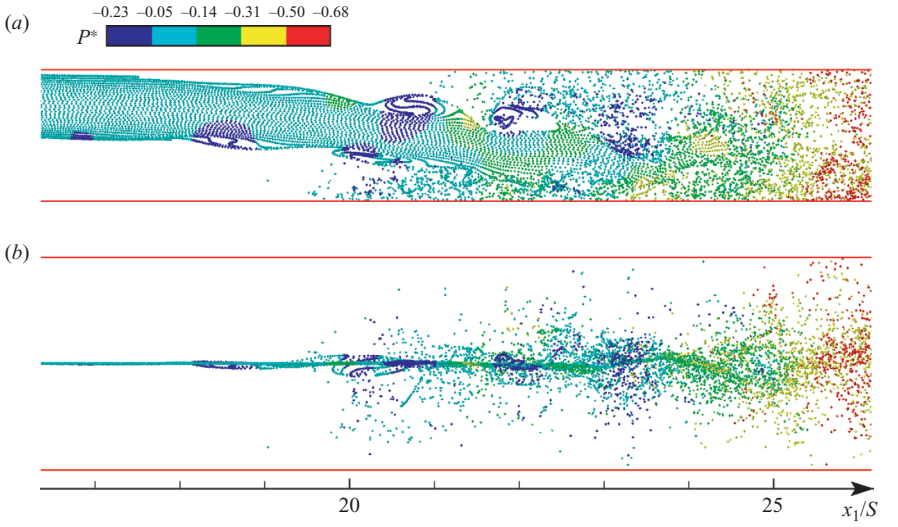

FIGURE 14. Zoomed view of particle traces released at source zone 1 in the area of transition from laminar to turbulent flow state; colour coding using the normalized pressure at the position of the particles ($P^* = P/\frac{\rho}{2}U_b^2$). For the sake of an enhanced accentuation of the pressure differences, the pressure interval shown was decreased. (*a*) Side view. (*b*) Top view.

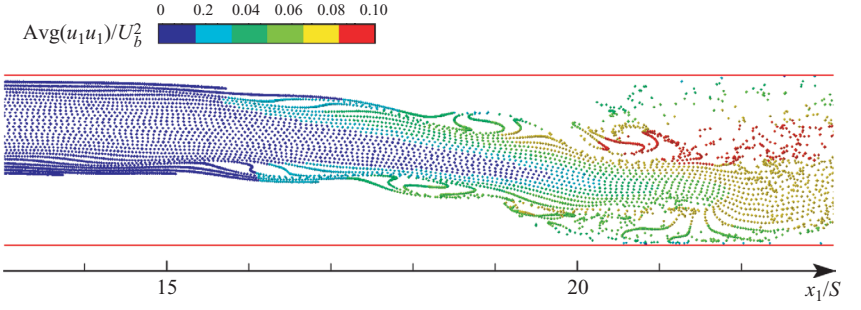

FIGURE 15. Selected streaklines released at source region 2 (side view); colour coding according to the dominating normal stress component $\overline{u_1u_1}$.

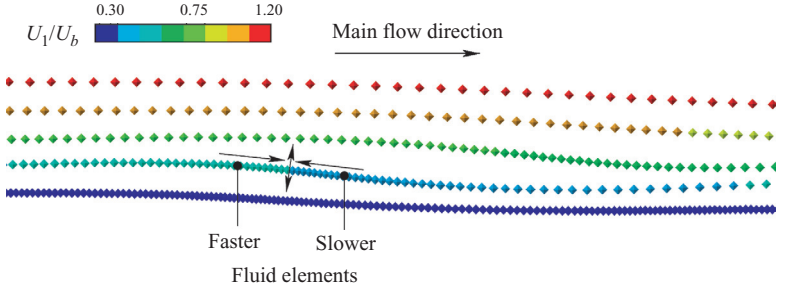

FIGURE 16. Widening of the streaklines in the shear layer between the main flow and the primary recirculation region (x_1–x_2 plane); colour coding according to the velocity component in the main flow direction.

https://doi.org/10.1017/S0022112008005235 Published online by Cambridge University Press

interval of $t\,U_b/S \approx 50$, vortices in the shear layers always emerge in pairs (one in the lower and one in the upper shear layer; see video 5 or 6). Accordingly, a staggered arrangement of the vortices can be observed in figure 15. In relation to the vortices in the lower shear layer, the corresponding vortices in the upper shear layer are shifted downstream in the main flow direction. Furthermore, it can be detected that the widening of the streaklines takes place in a restricted area which is surrounded by more or less undisturbed fluid. A widening of the streaklines is evident in most cases already at $x_1/S \approx 11$, whereas the roll-up of the vortical structures takes place at first in the region $15 < x_1/S < 17$ for the lower shear layer or in the area $16 < x_1/S < 18$ for the upper shear layer. However, as is visible in the animations, occasionally strong delays in the widening of the streaklines and the roll-up of the vortices are observed. Thus certain irregularities in the vortex generation are found. The period length and the time histories of the x_1-location, at which the vortices are emerging, show distinct fluctuations. The mean frequency for the development of vortices derived from the animations is determined as $St \approx 0.27$.

The physical mechanism leading to the widening of the streaklines in the shear layers is obvious in figure 16. Since the particles are moving within a shear layer comprising a vertical velocity gradient $\partial U_1/\partial x_2$, the corresponding particles in neighbouring streaklines possess different velocities. If now streaklines are displaced upwards or downwards in the vertical direction due to a local perturbation (as is the case for the second and third streakline from bottom in figure 16), the particles receive minor velocity differences along the streaklines, resulting from the vertical velocity gradient. In a situation as shown in figure 16, the slower particles within a perturbed streakline are located downstream of the faster particles. Therefore, the distance between the particles decreases in time, which becomes obvious if the second and third streaklines are followed in the main flow direction. Since the basically pointwise particles represent the location of fluid elements, it means that fluid elements are locally compressed in the streamwise direction. Since the fluid considered is assumed to be incompressible, it has to swerve in the vertical direction (the flow is quasi two-dimensional in this region), leading to the spreading of the streaklines. Thereby the upwards and downwards displacement of the streaklines is strengthened, resulting in larger velocity differences along the streaklines. Correspondingly, the fluid elements are further compressed in the main flow direction, and the streaklines are further spread until finally a roll-up of the shear layer sets in. Thus, it is a self-amplifying process which is initiated by minor vertical fluctuations in the shear layer. In contrast to this process, stabilizing mechanisms which try to compensate the velocity differences are evident. The most important one is given by the molecular momentum transport owing to the viscosity of the fluid. Hence whether a marginal vertical perturbation of the fluid will be damped or will lead to roll-up of the shear layer depends on the interplay between stabilizing and destabilizing forces.

Corresponding fluctuations of the flow field are already developing in the vicinity of the step and are amplified during their convective transport in the downstream direction. An exponential growth rate of the instantaneous fluctuations is found in the streamwise direction for a large area behind the step. This observation can be made based on time histories of the flow field recorded at fixed spatial positions. The locations are chosen in such a manner that they comprise all relevant regions of the flow; the coordinates are given by $x_1/S = 0.1, 1.1, 5.3, 10.6, 15.9, 21.2, 26.5, 31.8$, $x_2/S = -2/3, -1/3, 0, 1/3, 2/3$ and $x_3 = B/2$. The values of the flow variables at these points are determined by trilinear interpolation and recorded in time.

https://doi.org/10.1017/S0022112008005235 Published online by Cambridge University Press

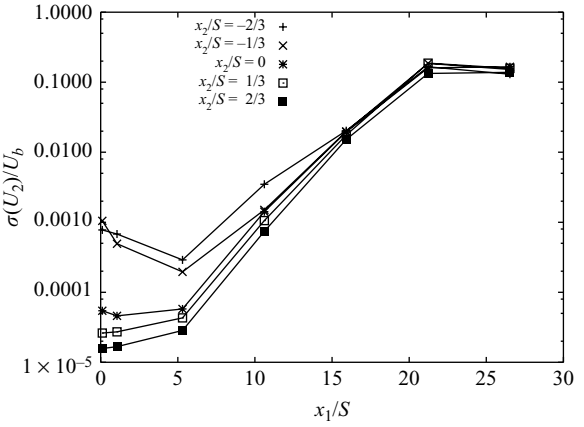

FIGURE 17. Standard deviation σ of the instantaneous fluctuations of the velocity component U_2 at various points in the flow domain. The top two graphs partially pass through the primary recirculation region, where in a wide range the instantaneous fluctuations of the flow field are stronger than in the main flow.

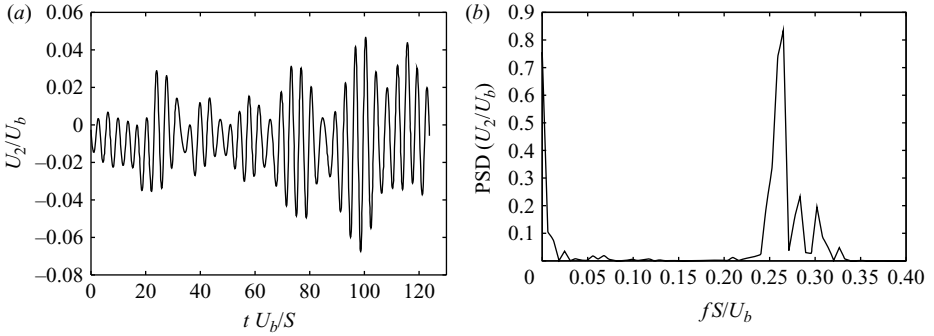

FIGURE 18. Oscillations of the U_2 velocity component at location $(x_1/S, x_2/S) = (15.9, -1/3)$ (initial time $t = 0$ arbitrarily chosen). PSD denotes power spectral density (*a*) Time series. (*b*) Power spectrum.

Figure 17 shows the standard deviations of the instantaneous fluctuations of the velocity component U_2 versus the distance from the step. In a wide spatial range an exponential growth of the fluctuations can be observed. The fluctuations of the U_2 velocity play an important role, since they represent an indication of vertical fluid movement and thus reflect the widening and roll-up of the shear-layer vortices.

The oscillations of the velocity field at the position $(x_1/S, x_2/S) = (15.9, -1/3)$, which is located below the channel centreline at a distance of several step heights prior to the end of the primary recirculation region, are exemplarily displayed in figure 18(*a*). The oscillations show a behaviour typical for a beat, which is a clear hint for the superposition of several frequencies of nearly the same value. This finding is supported by the frequency spectrum depicted in figure 18(*b*). It shows that the most important frequency contributions can be found at the Strouhal numbers $St = f\,S/U_b \approx 0.26$, 0.28 and 0.30. The strongest contribution is detected at $St \approx 0.26$, whereas the two other contributions are significantly weaker than the dominating frequency.

https://doi.org/10.1017/S0022112008005235 Published online by Cambridge University Press

A similar beat-like behaviour can also be observed for the other locations considered, provided that they are located prior to the transition to turbulence. These beat-like fluctuations found in the time histories represent certain irregularities of the vortex development process in the shear layers appearing from time to time. This phenomenon has already been mentioned above. The mean frequency of the vortex development derived from animations ($St \approx 0.27$) agrees well with the frequency contributions detected in the time series of the U_2 velocity component, which are characterized by a dominating contribution at $St \approx 0.26$ and two weaker contributions at $St \approx 0.28$ and 0.30. The results indicate that the different frequency contributions are already present directly past the step and are amplified in the shear layers during their convective transport in streamwise direction.

7.2.3. *Interaction between the shear-layer vortices and the recirculation regions*

The mean frequency of the vortex development in the shear layers determined in the preceding section ($St \approx 0.27$) coincides well with the mean frequency of the oscillations of the recirculation regions ($St \approx 0.266$) found in § 7.2.1. This is a clear hint for a correlation between the shear-layer vortices and the oscillations of the recirculation regions to be investigated in detail in the subsequent section applying the co-visualization technique.

Figure 19 depicts streaklines released from source zone 2 past the step and isosurfaces of vanishing U_1 velocity component representing the recirculation regions. It is obvious that those zones of negative fluid velocity which are visible at the upper channel wall at the beginning of the secondary recirculation region correspond to the vortices emerging in the upper shear layer. Although only an insignificant widening of the streaklines can be detected at $x_1/S \approx 15$, a region of recirculating fluid characterized by negative U_1 velocity evolves above the streaklines at the wall. The regions of backward-flowing fluid are convected downstream together with the emerging vortices. During this process, the streaklines roll up more and more, and the region of negative fluid velocity located above the vortex grows significantly in size (compare the corresponding animation 7).

The interaction between the vortices in the lower shear layer and the primary recirculation region is shown in more detail in figure 20. In order to present the vortex movement more clearly, the particles are no longer displayed by points but by velocity vectors indicating the local direction of fluid movement. To avoid overloading the figure, the arrowheads of the velocity vectors are omitted. However, since the vortices are moving downstream convectively, this measure is not sufficient to visualize the vortex movement distinctly. It is well known that both vector and streamline representations are not always capable of visualizing vortices in instantaneous flow fields (Lane 1995). This is especially true if vortices are moving with some convection velocity. Thus, the mean convection velocity is subtracted from the instantaneous velocity vector, and the resulting relative flow field showing the rotational movement of the particles around the vortex core is depicted in figure 20. For that purpose, the mean convection velocity U_c is taken over from the investigations on the pressure isosurfaces in § 7.2.2 ($U_c = 0.63\,U_b$ for the vortices in the lower shear layer).

Based on figure 20, it is obvious that the oscillations of the primary recirculation region are caused by vortical structures which originally emerged from the lower shear layer and pass by convectively. This behaviour can also be seen in animations which were generated for a longer time interval. Figure 20(*a*) depicts several vortices in which vortex A is located just at the reattachment region of the primary recirculation zone. It is a vortex which rotates in the clockwise direction. Hence the fluid between

https://doi.org/10.1017/S0022112008005235 Published online by Cambridge University Press

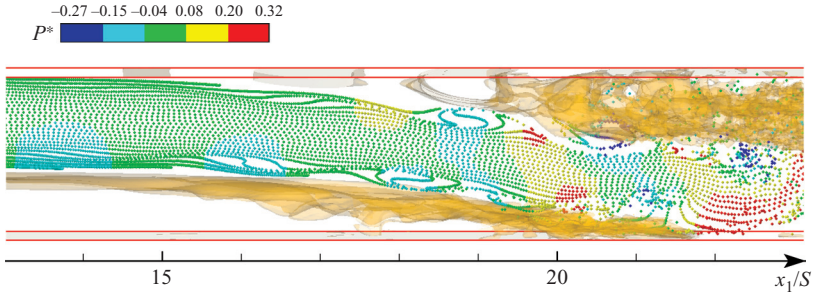

FIGURE 19. Interaction between vortical structures in the shear layers and the recirculation regions; the latter are displayed by isosurfaces of vanishing U_1 velocity component (particles released from source zone 2; colour coding according to the normalized pressure $P^* = P/(\rho/2)U_b^2$ at the position of the particle); compare also video 7.

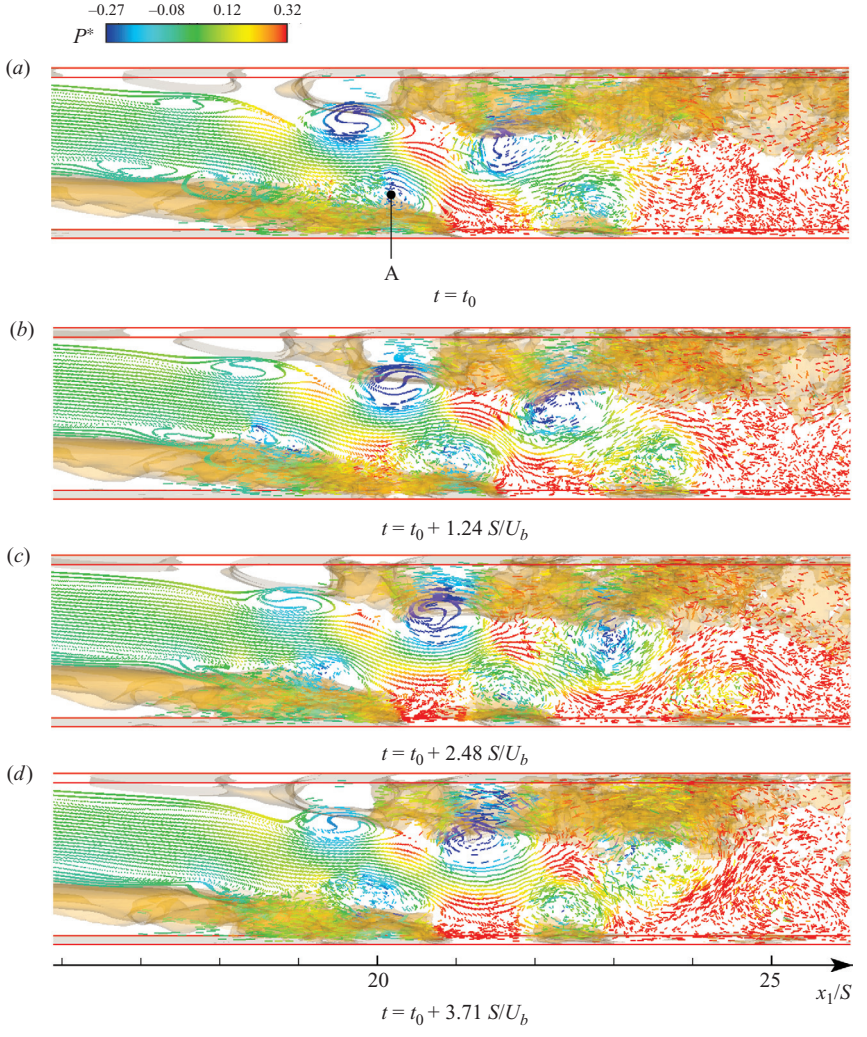

FIGURE 20. Interaction between the vortical structures in the shear layers and the recirculation regions (particles released from source region 2; colour coding corresponding to the normalized pressure $P^* = P/(\rho/2)U_b^2$ at the position of the particle); compare also video 8.

https://doi.org/10.1017/S0022112008005235 Published online by Cambridge University Press

the vortex core and the lower channel wall moves in the negative x_1-direction, leading to an area of backward-flowing fluid below the vortex. Owing to the convective transport of the vortex in the main flow direction, the region of negative U_1 velocity at the lower side of the structure is shifted downstream, yielding a recirculation region which increases in time (figure 20*b*). The nearly linear growth rate of the recirculation region observed in figure 11 is a direct result of a substantially constant convection velocity of the vortices. During the ongoing development, the vortex moves further downstream, whereas the area of backward-flowing fluid at the lower side of the vortex remains and separates from the original recirculation region (figure 20*c*). Now relatively fast-moving fluid from the main flow hits the lower channel wall. As a consequence, a region with positive U_1 velocity evolves, and therefore the length of the recirculation region suddenly drops. This phenomenon explains the saw-toothed behaviour observed for the reattachment length of the primary recirculation region found in figure 11.

Figure 21 illustrates that the vortical structures emerging from the lower shear layer show a relatively complex behaviour when passing the primary recirculation region. Particles within the rolling up vortices were manually chosen to analyse their transport in the downstream direction. Whereas the vortices in the upper shear layer are transported downstream without being hindered, a significant delay can be detected for the vortices in the lower shear layer in front of the reattachment area of the primary recirculation region (vortex A; see figure 21*b*, *c*). Although some fluid elements are picked up by a preceding vortex not shown here, most of the fluid elements from the core of vortex A remain behind, so that a clearly visible interaction with the subsequent vortex B takes place (figure 21*c*). However, vortex pairing is not detected. Instead, the subsequent vortex B is also delayed, whereas vortex A continues its movement in the downstream direction, leading to the next oscillation of the reattachment region (figure 21*d*, *e*).

To analyse the interaction of the shear-layer vortices with the recirculation regions more thoroughly, particles were also injected within the recirculation regions. The results for the source zones 3 and 4, which range along the channel walls in the x_3-direction in the reattachment area of the recirculation regions (compare figure 13), are presented in figure 22. As the corresponding animations clearly show, the shear-layer vortices assimilate larger amounts of fluid from the separation zones when passing the recirculation regions and transport this fluid downstream (see videos 9 and 10). Based on this mechanism, especially the vortices in the upper shear layer interact strongly with the secondary recirculation region. Moreover, video 9 reveals that fluid elements at the front part of the secondary separation region exhibit significant oscillations in the x_1-direction. Simultaneously, zones of locally increased and decreased pressure can be detected, which march through the secondary recirculation region, while the shear-layer vortices pass by.

The above oscillations of the fluid elements next to the top wall are related to the zones of negative and positive fluid velocities, which move alternately along the upper channel wall and are noticeable by isosurfaces of the isovalue $U_1 = 0$ (see figure 19). The time histories of the streamwise position $x_{1,p}$ of a selected particle p released from source zone 4 within the secondary recirculation region are depicted in figure 23(*a*). As is clearly visible, the particle departs from its origin in the negative x_1-direction until the movement decelerates, and increasingly slight oscillatory fluctuations of the particle position occur. These oscillations can also be detected in the time history of the particle velocity $U_{1,p}$ displayed in figure 23(*b*). In order to identify the dynamic

https://doi.org/10.1017/S0022112008005235 Published online by Cambridge University Press

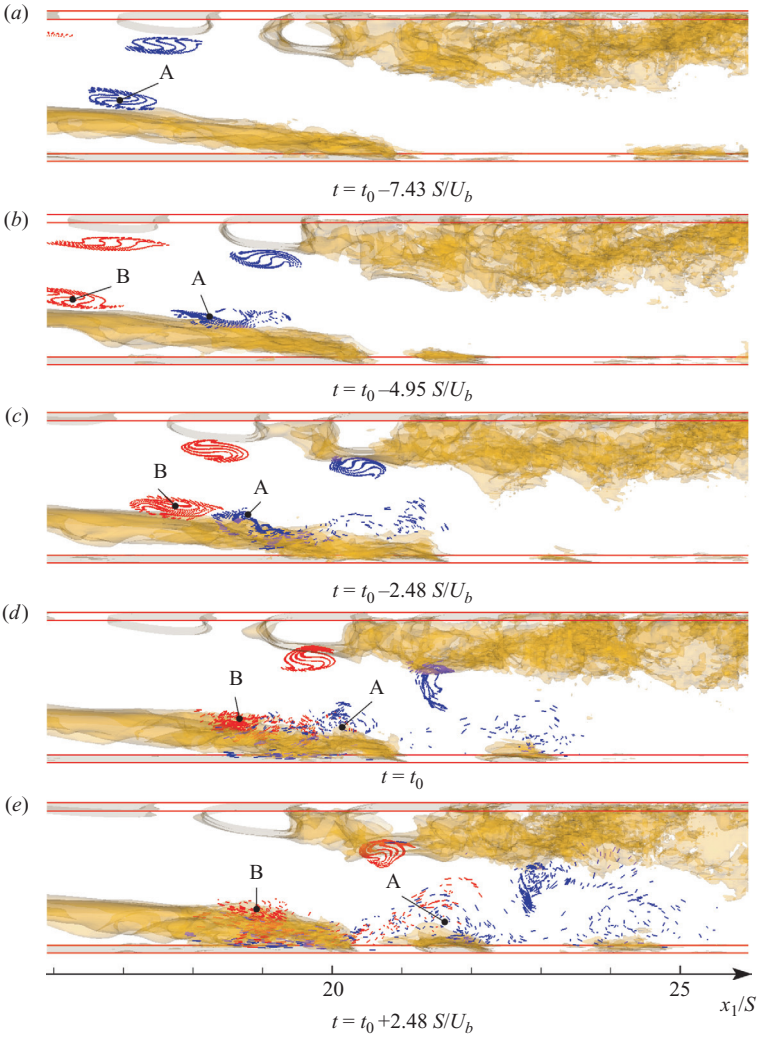

FIGURE 21. Visualization of selected vortices and their interaction in the area of the reattachment of the primary recirculation region (t_0 as in figure 20). Vortices which evolve at the same time are given in the same colour.

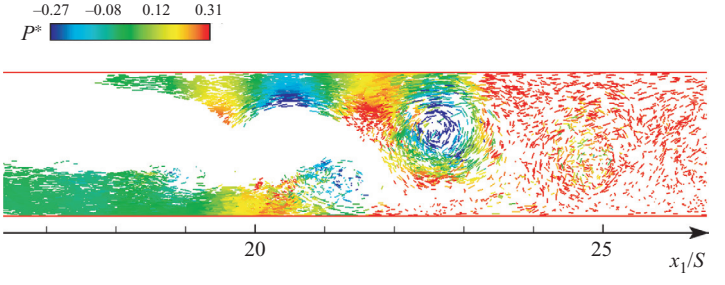

FIGURE 22. Particles released from source zones 3 and 4, which are located close to the channel walls within the recirculation regions. Particle representation by tangents of the velocity field at the location of the particle (velocity relative to the mean convection velocity of the shear-layer vortices).

https://doi.org/10.1017/S0022112008005235 Published online by Cambridge University Press

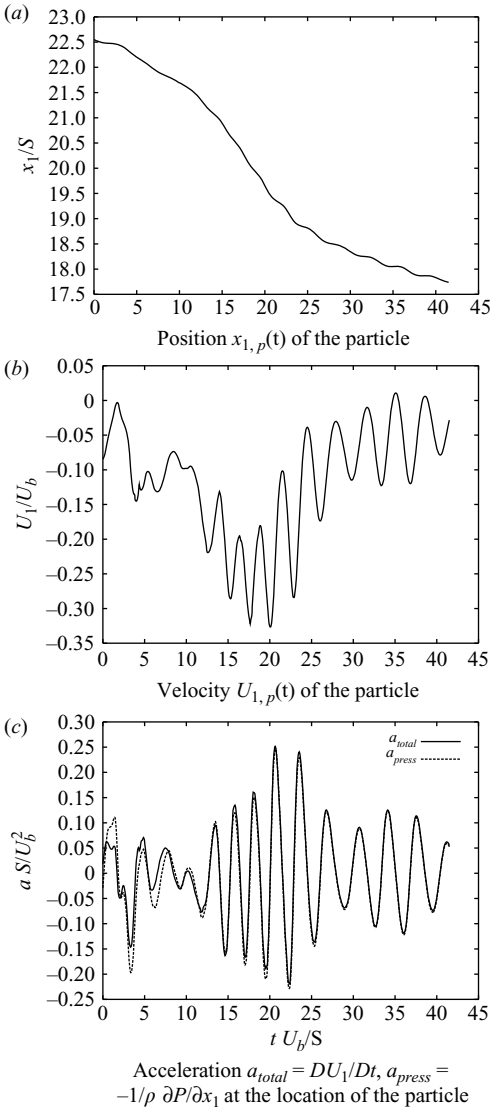

FIGURE 23. Time histories of the position, the velocity and the acceleration (all in the x_1-direction) of a selected particle released at source zone 4 within the secondary recirculation region.

cause of these oscillations, the different contributions to the acceleration of the particles were investigated more deeply. These contributions can be derived from the velocity and pressure fields in the following manner: Since the pointwise particles considered here for streakline generation are assumed to be massless and with zero extension, such a particle always moves with the same velocity as the fluid at the particle position. Thus the particle represents the location of a fluid element f. Consequently, the location $x_{i,p}(t)$ and the velocity $U_{i,p}(t)$ of the particle are identical with the location $x_{i,f}(t)$ and the velocity $U_{i,f}(t)$ of the fluid element. Therefore, the acceleration of the particle is related to the Eulerian field variables U_i and P in the

https://doi.org/10.1017/S0022112008005235 Published online by Cambridge University Press

following way:

$$\begin{aligned}\frac{\mathrm{d}U_{j,p}(t)}{\mathrm{d}t} = \frac{\mathrm{d}U_{j,f}(t)}{\mathrm{d}t} &= \frac{\mathrm{d}}{\mathrm{d}t}U_j(x_i,t), \quad x_i = x_{i,f}(t)\\ &= \frac{\partial U_j}{\partial t} + \frac{\partial U_j}{\partial x_i}\frac{\mathrm{d}x_{i,f}}{\mathrm{d}t}, \quad \frac{\mathrm{d}x_{i,f}}{\mathrm{d}t} = U_{i,f} = U_i\\ &= \frac{\partial U_j}{\partial t} + U_i\frac{\partial U_j}{\partial x_i}\\ &= \frac{\mathrm{D}U_j}{\mathrm{D}t} = -\frac{1}{\rho}\frac{\partial P}{\partial x_j} + \nu\frac{\partial^2 U_j}{\partial x_i^2}. \end{aligned} \tag{7.1}$$

Within the last step, a form of the momentum equation was applied, which was derived from (3.2), taking (3.3) and the incompressibility condition (3.1) into account. Accordingly, the substantial derivative $\mathrm{D}U_j/\mathrm{D}t$ at the location of the particle describes the total acceleration of the particle; the term $-1/\rho\,\partial P/\partial x_j$ at the location of the particle expresses the acceleration due to pressure forces. Both acceleration terms were evaluated for the selected particle based on the velocity and pressure fields, using finite differences. Then they were trilinearly interpolated to the location of the particle. An approximation of first-order accuracy was applied for the temporal derivative, and approximations of second-order accuracy were chosen for the spatial derivatives.

The outcome of this analysis is composed in figure 23(*c*). It is clearly visible that the acceleration of the particle in the front part of the recirculation region ($t\,U_b/S > 25$) is more or less exclusively caused by the pressure gradient. This means that the zones of negative U_1 velocity in the front part of the secondary recirculation region, which according to figure 19 correspond to the vortices in the upper shear layer, are provoked by pressure gradients. These gradients are produced as follows: Each vortex in the upper shear layer is connected to a local pressure minimum which ranges up to the upper wall; on the other hand a local pressure maximum exists between two consecutive vortices. As the vortices are moving downstream, a sequence of local pressure minima and maxima travels with the vortices through the secondary recirculation region. Correspondingly, an oscillating pressure gradient results, which alternately accelerates the fluid elements in the negative and positive x_1-directions. By this means, regions of negative and positive U_1 velocities are generated at the upper channel wall. Owing to the phase shift between the acceleration and the resulting velocity (compare figure 23*b* and 23*c*) the minimum or maximum of the velocity is just reached when the pressure gradient vanishes. This is true for the pressure minimum (i.e. above a shear-layer vortex) and the pressure maximum, respectively. Therefore, the regions of negative U_1 velocity are exactly located above the shear-layer vortices.

It can be concluded that the oscillations of the primary and the secondary recirculation regions are related to the vortical structures evolving in the shear layers. Furthermore, the mechanisms causing these oscillations have been identified. In the case of the separation point of the secondary recirculation region, pressure fluctuations emerging from the vortices in the upper shear layer and leading to oscillations of the fluid velocity at the upper channel wall are responsible for the flow behaviour observed. In principle, the same effects play a role in the oscillations of the reattachment point at the lower channel wall, since a sequence of local pressure minima and maxima is also connected to the vortical structures in the lower shear layer. However, the main contribution is afforded here by the rotational movement of the vortex striking the lower channel wall. The rotation induces a zone of negative fluid velocity at the lower side of the vortex. Of course, the rotational movement of

https://doi.org/10.1017/S0022112008005235 Published online by Cambridge University Press

the fluid at the bottom wall is also induced by pressure forces, since it is the pressure difference between the vortex core and the surrounding fluid which keeps the fluid elements on their rotating trajectories. However, there is an important qualitative difference between the situation at the lower wall and the upper wall. While the vortices in the lower shear layer are hitting the bottom wall, the vortices of the upper shear layer move away from the top wall so that no fluid rotating and moving downstream with the vortex is able to reach the wall. The fluid in the front part of the secondary recirculation region is moving back and forth as indicated by figure 23 (see also video 9), but it is mostly not carried downstream by the shear layer vortices. This situation is very different from that at the bottom wall. Obviously, the pressure forces induced by a vortex core in the upper shear layer have a more far-reaching influence than the rotational movement of the vortex itself.

The fact that no vortex pairing is found in the present work is in accordance with the finding that the frequency of the oscillations of the recirculation region is equal to the frequency observed for the development of the shear-layer vortices. Vortex pairing would change the frequency of the flapping behaviour, since in the case of vortex pairing and merging of two vortices the number of vortices passing the recirculation region in a certain time span would be reduced. This is possibly the reason why in other investigations considering an external backward-facing step flow in the fully turbulent regime significantly smaller Strouhal numbers of the oscillation of the primary reattachment length were found ($St \approx 0.06$, Le *et al.* 1997; $St = 0.07$, Métais 2001; $St \approx 0.27$, present work). In Métais (2001) the Strouhal number of the Kelvin–Helmholtz vortices developing in the shear layer was calculated as 0.23, which reduced to 0.12 after helical pairing. Unfortunately, it is not clear whether a second vortex pairing event took place in the considered flow case. This would further reduce the Strouhal number of the vortices to about 0.06, which is approximately the oscillation frequency of the reattachment length. Further investigations in this direction should be undertaken in order to determine the exact frequency of the shear layer vortices when passing the end of the recirculation region.

8. Conclusion and final remarks

In this paper, a detailed analysis of the dynamic processes taking place in an internal flow past a backward-facing step in the transitional regime has been presented. As known from the literature, the backward-facing step flow is prone to oscillations of the reattachment length of the primary recirculation region, also denoted 'flapping'. Although the term flapping most commonly refers to overall oscillations of separated shear layers, the focus of the present work was on the flapping of the reattachment and separation lines. The mechanisms leading to this ocillatory behaviour were investigated in detail by analysing the time-dependent flow, using co-visualization techniques. In addition to the oscillations of the primary reattachment line, oscillations of the separation and the reattachment line of the secondary recirculation bubble at the upper channel wall were also observed. The investigations clearly show that the flapping of the primary reattachment and the secondary separation line is due to vortical structures in the unstable shear layers between the main flow and the recirculation bubbles. The shear layer vortices are swept downstream convectively, and while passing the recirculation regions they induce small zones of backward-flowing fluid at the channel walls. These zones of negative fluid velocity move downstream together with the shear-layer vortices. The dynamic origin of these zones was studied. In the case of the primary recirculation region, it was mainly the rotational movement

https://doi.org/10.1017/S0022112008005235 Published online by Cambridge University Press

of the shear-layer vortices impinging on the lower channel wall which caused the zones of negative fluid velocity. In the case of the secondary recirculation region, however, the shear-layer vortices were moving away from the upper channel wall, so that the rotational movement of the vortices did not reach the boundary. Here, pressure gradients originating from local pressure minima located in the shear-layer vortex cores were identified as being responsible for the oscillations of the separation line at the upper channel wall. These pressure gradients, which move downstream with the shear-layer vortices, were found to have an influence up to the top boundary of the computational domain and to create alternating zones of backward- and forward-flowing fluid along the wall. These unsteady processes were documented in the form of several animations which are available online, journals.cambridge.org/FLM.

It is worth noticing that the local flapping of the reattachment and separation lines investigated in the present work and the overall flapping of the shear layers mentioned above are possibly just two sides of the same coin. The shear layer vortices causing the oscillation of the reattachment and the separation zones might also cause an overall oscillation of the shear layers, where the vortices are generated. This is indicated by transverse velocity ocillations in the shear layers found in the present study. However, more investigations have to be done in this direction to clarify this issue.

Closely related to this question is the observation that the Strouhal number found for the oscillation of the primary reattachment line was significantly higher in the present flow case than in studies of external backward-facing step flows in the turbulent regime. In the present investigation, vortex roll-up in the shear layers and flapping of the reattachment line happened at the same Strouhal number. No vortex pairing occurred in the shear layers which could have reduced the Strouhal number of the reattachment line oscillation. However, vortex pairing is reported in other studies in the turbulent regime, which contributes to the smaller Strouhal numbers of the flapping reattachment line found there. Further work is necessary to clarify this issue and to identify the precise mechanisms of vortex roll up, vortex pairing and flapping of the reattachment line in the turbulent regime.

The investigations clearly showed that the backward-facing step flow is extremely sensitive to numerical errors (e.g. grid-induced oscillations) and the choice of the inflow boundary conditions, especially in the transitional regime. Accordingly, a careful grid design is very important for an accurate prediction of the flow field developing downstream of the step. Too low a grid resolution might lead to a significant underprediction of the separation and reattachment lengths.

In order to analyse the different transient mechanisms characterizing the backward-facing step flow, a co-visualization approach was adopted. Based on this technique, it was possible to investigate transient processes at high temporal resolution and in all detail. The analysis covered a time window of length $tU_b/S \approx 50$, corresponding to about 1.5 flow-throughs. During this time period, a total of 19.8 gigabyte particle data and 25.3 gigabyte isosurface data were produced. Thus, the costs in terms of storage space were very moderate so that the time-dependent flow behaviour was analysed in a very efficient way. Using traditional post-processing techniques, this is extremely difficult to achieve or may not even be possible at all, since it would be necessary to store about 2.6 terabyte of flow solution in order to yield a visualization at the same temporal resolution. This corresponds to a data-reduction factor of 74:1 obtained by the co-visualization approach.

The calculation of particle traces for streakline generation proved to be extremely useful in the analysis of the flow. Since the calculation of traces of massless and volumeless particles leads from an Eulerian to a Lagrangian description of the flow, a

https://doi.org/10.1017/S0022112008005235 Published online by Cambridge University Press

detailed analysis of the forces which are responsible for the acceleration of single fluid elements was allowed for. This can be easily extended to other applications, where additional forces such as surface forces due to Marangoni convection and Lorentz forces due to magnetic fields occur.

The present work was carried out as part (TP C3) of the Centre of Excellence SFB 603 'Model-Based Analysis and Visualisation of Complex Scenes and Sensor Data' at the University of Erlangen–Nuremberg. Financial support by the Deutsche Forschungsgemeinschaft is gratefully acknowledged.

REFERENCES

Argyris, J. & Schlageter, H. U. 1996 Parallel interactive and integrated visualization. In *Flow Simulation with High-Performance Computers II: Notes on Numerical Fluid Mechanics* (ed. E. H. Hirschel), vol. 52, pp. 184–202. Vieweg.

Armaly, B. F., Durst, F., Pereira, J. C. F. & Schönung, B. 1983 Experimental and theoretical investigation of backward-facing step flow. *J. Fluid Mech.* **127**, 473–496.

Barkley, D., Gomes, M. G. M. & Henderson, R. D. 2002 Three-dimensional instability in flow over a backward-facing step. *J. Fluid Mech.* **473**, 167–190.

Basu, B., Enger, S., Breuer, M. & Durst, F. 2000 Three-dimensional simulation of flow and thermal field in a Czochralski melt using a block-structured finite-volume method. *J. Cryst. Growth* **219** (1–2), 123–143.

Binninger, B. 1989 Untersuchung von Modellströmungen in Zylindern von Kolbenmotoren. (in German). PhD thesis. Aerodynamisches Institut, RWTH Aachen.

Biswas, G., Breuer, M. & Durst, F. 2004 Backward-facing step flows for various expansion ratios at low and moderate Reynolds numbers. *J. Fluids Engng* **126**, 362–374.

Blackburn, H. M., Barkley, D. & Sherwin, S. J. 2008 Convective instability and transient growth in flow over a backward-facing step. *J. Fluid Mech.* **603**, 271–304.

Breuer, M. 2002 *Direkte Numerische Simulation und Large-Eddy Simulation turbulenter Strömungen auf Hochleistungsrechnern: Habilitationsschrift, Universität Erlangen-Nürnberg, Berichte aus der Strömungstechnik*. Shaker.

Chiang, T. P. & Sheu, T. W. H. 1999 A numerical revisit of backward-facing step flow problem. *Phys. Fluids* **11** (4), 862–874.

Delcayre, M. & Lesieur, M. 1997 Topological feature in the reattachment region of a backward-facing step. In *First AFOSR Intl Conf. on DNS and LES*, Ruston, Los Angeles.

Durst, F. & Schäfer, M. 1996 A parallel block-structured multigrid method for the prediction of incompressible flows. *Intl J. Numer. Meth. Fluids* **22**, 549–565.

Durst, F., Schäfer, M. & Wechsler, K. 1996 Efficient simulation of incompressible viscous flows on parallel computers. In *Flow Simulation with High-Performance Computers II: Notes on Numerical Fluid Mechanics* (ed. E. H. Hirschel), vol. 52, pp. 87–101. Vieweg.

Eaton, J. K. & Johnston, J. P. 1980 Turbulent flow reattachment: an experimental study of the flow and structure behind a backward-facing step. *Tech Rep.* MD-39. Thermosciences Division, Department of Mechanical Engineering, Stanford University.

Enger, S. 2001 Numerical simulation of flow and heat transfer in Czochralski crucibles. PhD thesis. Lehrstuhl für Strömungsmechanik, Universität Erlangen–Nürnberg.

Enger, S., Gräbner, O., Müller, G., Breuer, M. & Durst, F. 2001 Comparison of measurements and numerical simulations of melt convection in Czochralski crystal growth of silicon. *J. Cryst. Growth* **230** (1–2), 135–142.

Friedrich, R. & Arnal, M. 1990 Analysing turbulent backward-facing step flow with the lowpass-filtered Navier–Stokes equations. *J. Wind Engng Indus. Aerodyn.* **35**, 101–128.

Globus, A. 1992 A software model for visualization of large unsteady 3-D CFD results. *Tech Rep.* RNR-92-031. NASA Ames Research Center.

Grosso, R., Wechsler, K., Ertl, T. & Schäfer, M. 1996*a* Computational steering and visualization for multiblock multigrid flow simulations. In *High-Performance Computing and Networking: Lecture Notes in Computer Science* **1067** (ed. H. Liddell, A. Colbrook, B. Hertzberger & P. Sloot), pp. 927–928. Springer.

https://doi.org/10.1017/S0022112008005235 Published online by Cambridge University Press

Grosso, R., Schulz, M., Kraheberger, J. & Ertl, T. 1996*b* Flow visualization for multiblock multigrid simulations. In *Virtual Environments and Scientific Visualization '96* (ed. P. Slavick & J. J. van Wijk), pp. 143–152. Springer.

Haimes, R. 1994 pV3: A. distributed system for large-scale unsteady CFD visualization. *AIAA Paper* 94-0321. American Institute of Aeronautics and Astronautics.

Kaiktsis, L., Karniadakis, G. E. & Orszag, S. A. 1991 Onset of three-dimensionality, equilibria, and early transition in flow over a backward-facing step. *J. Fluid Mech.* **231**, 501–528.

Kaiktsis, L., Karniadakis, G. E. & Orszag, S. A. 1996 Unsteadiness and convective instabilities in two-dimensional flow over a backward-facing step. *J. Fluid Mech.* **321**, 157–187.

Kaltenbach, H.-J. & Janke, G. 2000 Direct numerical simulation of flow separation behind a swept, rearward-facing step at $Re_H = 3000$. *Phys. Fluids* **12** (9), 2320–2337.

Khier, W., Breuer, M. & Durst, F. 2000 Flow structure around trains under side wind conditions: a numerical study. *Intl J. Comp. Fluids* **29** (2), 179–195.

Lane, D. A. 1995 Visualization of numerical unsteady fluid flows. *Tech Rep.* NAS-95-017. NASA Ames Research Center.

Le, H., Moin, P. & Kim, J. 1997 Direct numerical simulation of turbulent flow over a backward-facing step. *J. Fluid Mech.* **330**, 349–374.

Lee, T. & Mateescu, D. 1998 Experimental and numerical investigation of 2-D backward-facing step flow. *J. Fluids Struct.* **12**, 703–716.

Lorensen, W. E. & Cline, H. E. 1987 Marching cubes: A high resolution 3D surface construction algorithm. *Comp. Graphics* **21** (4), 163–169.

Manzano, N., Walle, F. & Vandromme, D. 1996 ATM used for CFD visualization: preliminary experiments. In *Proc. of the French-German Workshop on Computation and Visualization of 3-D Vortical and Turbulent Flows*. Technische Universität München.

Métais, O. 2001 Large-eddy simulation of turbulence. In *New Trends in Turbulence* (ed. M. Lesieur, A. Yaglom & F. David), pp. 117–186. Springer.

Moffat, H. K. 1964 Viscous and resistive eddies near a sharp corner. *J. Fluid Mech.* **18**, 1–18.

Nie, J. H. & Armaly, B. F. 2002 Three-dimensional convective flow adjacent to backward-facing step: effects of step height. *Intl J. Heat Mass Transfer* **45**, 2431–2438.

Rhie, C. M. & Chow, W.L. 1983 A numerical study of the turbulent flow past an isolated airfoil with trailing edge separation. *AIAA J.* **21**, 1525–1532.

Scarano, F. & Riethmuller, M. L. 2000 Temporal analysis of coherent structures in a turbulent BFS flow with PIV. In *10th Intl Symp. on Applications of Laser Techniques to Fluid Mechanics*, Lisbon, Portugal.

Schäfer, F. & Breuer, M. 2002 Comparison of c-space and p-space particle tracing schemes on high-performance computers: accuracy and performance. *Intl J. Numer. Meth. Fluids* **39**, 277–299.

Schäfer, F., Kumar, V., Breuer, M. & Durst, F. 2005 Visualization and computational steering of fluid motion in Czochralski crucibles during silicon crystal growth. *Intl J. Comput. Fluid Dyn.* **19** (7), 501–515.

Stone, H. L. 1968 Iterative solution of implicit approximations of multidimensional partial differential equations. *SIAM J. Num. Anal.* **5**, 530–558.

Williams, P. T. & Baker, A. J. 1997 Numerical simulations of laminar flow over a 3D backward-facing step. *Intl J. Numer. Meth. Fluids* **24**, 1159–1183.

https://doi.org/10.1017/S0022112008005235 Published online by Cambridge University Press